LUT
Lappeenranta
University of Technology

Aki Pulkkinen

TOWARDS A BETTER UNDERSTANDING OF ACTIVITY AND SELECTIVITY TRENDS INVOLVING K AND O ADSORPTION ON SELECTED METAL SURFACES

Thesis for the degree of Doctor of Science (Technology) to be presented with due permission for public examination and criticism in Auditorium 6311 at Lappeenranta University of Technology, Lappeenranta, Finland on the 18th of December, 2017, at noon.

Acta Universitatis
Lappeenrantaensis 787

Supervisor Docent Katariina Pussi
LUT School of Engineering Science
Lappeenranta University of Technology
Finland

Reviewers Senior University Lecturer Jouko Lahtinen
Department of Applied Physics
Aalto University School of Science
Finland

Professor Karoliina Honkala
Department of Chemistry
University of Jyväskylä
Finland

Opponent Docent Jouko Nieminen
Department of Physics
Tampere University of Technology
Finland

ISBN 978-952-335-196-7
ISBN 978-952-335-197-4 (PDF)
ISSN 1456-4491
ISSN-L 1456-4491

Lappeenrannan teknillinen yliopisto
Yliopistopaino 2017

Abstract

Aki Pulkkinen
Towards a better understanding of activity and selectivity trends involving K and O adsorption on selected metal surfaces
Lappeenranta, 2017
52 p.
Acta Universitatis Lappeenrantaensis 787
Diss. Lappeenranta University of Technology
ISBN 978-952-335-196-7, ISBN 978-952-335-197-4 (PDF),
ISSN 1456-4491, ISSN-L 1456-4491

Oxidation reactions are the basis of many applications in chemical industry, and the reaction rates are increased by the presence of a suitable metallic surface that acts as a catalyst. The basic factor in explaining the reaction dynamics is the electronic structure of the catalyst and the reactants, which can be determined by modern computational methods. Typically, catalytic reactions on metal surfaces involve steps such as adsorption, dissociation, and diffusion. Understanding the elementary steps contributes to the overall understanding of catalytic properties of metal surfaces.

This study presents first-principles calculations of elementary processes on silver (110) and lead (100) surfaces. The preferred oxygen adsorption sites and the dissociation of the oxygen molecule on Ag(110) are clarified, and the diffusion and vibration of oxygen are analyzed.

On Pb(100) surface, potassium is shown to prefer substitutional adsorption sites and form an ordered structure at 0.5 monolayers coverage. Finally, the oxidation of Pb(100) surface results in a two layer oxide structure where oxygen occupies distorted hollow sites on and below the top surface layer.

Keywords: first principles calculations, surface physics, adsorption, oxidation

Acknowledgements

The research for this thesis was carried out in the group of computational materials science at Lappeenranta University of Technology between 2012–2017. First of all, I would like to thank my supervisor Katariina Pussi, whose determination played a major role in finishing this thesis. I also wish to thank my previous supervisor, Professor Matti Alatalo, for introducing me to the world of DFT. I am grateful for the advice provided by Professor Talat Rahman, Professor Emerita Renee Diehl and Professor Bernardo Barbiellini.

I would like to thank Professor Karoliina Honkala and Senior University Lecturer Jouko Lahtinen for their efforts as reviewers.

I thank my colleagues for the discussions that gave me other things to think about during the writing process.

Finally, I would like to express my gratitude to my family for their support. A special thanks goes to Elina, for always being there for me.

Lappeenranta, December 2017

Aki Pulkkinen

Contents

List of the original articles and the author's contribution

This thesis consists of an introductory part and three original, refereed articles in scientific journals. The articles and the author's contribution in them is summarized below.

I **T. B. Rawal, S. Hong, A. Pulkkinen, M. Alatalo, and T. S. Rahman**. Adsorption, diffusion and vibration of oxygen on Ag(110), *Physical Review B*, 92(3), p. 035444, 2015.

II **Y.-T. Huang, R. D. Diehl, A. Pulkkinen and K. Pussi**. Low-energy electron diffraction and density functional theory study of potassium adsorbed on Pb(100), *Journal of Physics: Condensed Matter*, 27(34), pp. 345001, 2015.

III **A. Pulkkinen and K. Pussi**. Atomic oxygen adsorption on Pb(100), *The European Physical Journal B*, 90(10), p. 184, 2017.

A. Pulkkinen is the principal author of paper III and has participated in writing papers I and II. He has calculated and analyzed the DFT results in papers II and III, and participated in the calculations and analysis of paper I.

Nomenclature

Symbols

a	lattice constant
e	elementary charge
E	energy
$\hbar$	reduced Planck constant
$\mathcal{H}$	Hamiltonian
m, M	mass
n	electron density
N	number of atoms
p	dipole moment density
Q	electric charge
$\boldsymbol{r}, \boldsymbol{R}$	position
T	temperature
ϕ	work function
ρ	charge density
σ	surface energy
Θ	coverage
Ψ	wavefunction

Acronyms

CINEB	climbing image nudged elastic band
DFT	density functional theory
DOS	density of states
EOS	equation of state
fcc	face-centered cubic
FFH	fourfold hollow
GGA	generalized gradient approximation
LB	long bridge
LDA	local density approximation
LEED	low-energy electron diffraction
MEP	minimum energy path
NEB	nudged elastic band
PAW	projector augmented wave
PBE	Perdew, Burke, and Ernzerhof
SB	short bridge
STM	scanning tunnelling microscopy
TFH	threefold hollow
TP	top
UHV	ultra-high vacuum
VASP	Vienna ab-initio simulation package

CHAPTER 1

Introduction

Atomic-scale phenomena at surfaces are of enormous technological importance. Corrosion is generally an undesired process, while atomic layer deposition and heterogeneous catalysis are essential processes in semiconductor manufacturing and chemical industry, respectively. These processes are at the interface of physics and chemistry. [1]

Many of the industrially relevant reactions are catalyzed by surfaces of transition metals, such as platinum, palladium, rhodium and ruthenium. A catalyst that is in different phase than the reactants is termed a heterogeneous catalyst. Typically, the catalytic reactions can be broken into a number of elementary steps. In the Langmuir-Hinshelwood mechanism, the reactants adsorb on the catalyst, and possibly dissociate [2]. The molecular fragments and atoms diffuse on the surface, form new bonds with each other, and the reaction products then desorb from the surface. An example of such a reaction is the catalytic oxidation of carbon monoxide to carbon dioxide [3]. In the Eley-Rideal mechanism, one of the reactants adsorbs on the surface, and the reaction takes place between the surface-adsorbed species and another reactant in gas phase [2]. The catalytic properties of surfaces are therefore closely related to the electronic structure of surfaces [4].

Key concepts in characterizing a catalyst are its *activity* and *selectivity* [2]. Activity refers to the ability of the catalyst to increase a reaction rate, which is related to the ability of the catalyst to adsorb reactants. However, the substrate-adsorbate bond should be strong enough for the adsorbate to cover the surface, but not too strong to immobilize or inactivate the reactants. For the surface to act as a catalyst, the reaction on the surface must have a lower energy barrier than in the gas phase. Same reactants can yield different products, depending on the catalyst. Such selectivity is essential in directing the reactions to desirable products.

The importance of the field is manifested by the acknowledgements awarded to the pioneers in the fields of heterogeneous catalysis and surface chemistry. Paul Sabatier received the Nobel prize in chemistry in 1912 “for hydrogenating organic compounds in the presence of finely disintegrated metals”, in other words a reaction involving heterogeneous catalysis. Later on, Irving Langmuir received the 1932 Nobel prize in chemistry for his re-

search in surface chemistry. The experimental work in the field and the understanding of surface reactions took a step forward in the 1960s when methods to produce ultra-high vacuum (UHV) became available, allowing to probe surfaces by e.g. low-energy electron diffraction (LEED). The understanding of chemical reactions at surfaces was strengthened by the work of Gerhard Ertl, for which he was awarded the 2007 Nobel prize in chemistry.

Computational surface science can act, on the one hand, as a support to the experiments, but also as a predictive tool. The theoretical foundations originate from the principles of quantum mechanics, formulated in the early twentieth century. However, direct application of the equations to real systems lead to intractable problems. In the 1960s, Walter Kohn showed that the ground state properties of a system can be determined from the electron density [5, 6], and John Pople led the field of computational quantum chemistry. They shared the 1998 Nobel prize in chemistry; Kohn for developing the density functional theory (DFT), and Pople for developing computational methods for quantum chemistry. At present, DFT is the most widely used method in computational surface science, and in-depth understanding of the individual steps of surface processes such as adsorption, dissociation and diffusion, are within the reach of computational surface science.

Silver is a common catalyst in catalytic oxidation reactions, that play a central role in various industrial processes [7]. Lead-based catalysts are less common, but lead oxides can catalyse e.g. peroxide decomposition [8] and methane dimerization [9, 10]. This book consists of computational studies of three adsorption systems that aim to build upon the understanding of the catalytic properties of Ag(110) and Pb(100) surfaces.

The rest of the book is organized as follows. Chapter 2 gives an outline of the theoretical methods employed by the software that is used to calculate the results, and Chapter 3 discusses the main results of the publications. Conclusions are given in Chapter 4.

CHAPTER 2

Overview of the computational methods

The main problem of modeling of materials at the atomic level is the description of the interactions of electrons with matter. The practical methods are always a compromise between accuracy and computational resources. Quantum chemistry methods tend to be based on the electronic wavefunctions, while the solid-state physics methods are mainly based on the electron density.

At the heart of the modeling of surfaces is the DFT, that offers good accuracy at a reasonable computational cost. The information acquired by DFT itself, ground state energy and electron density, is seldom enough in explaining the properties of materials and processes at surfaces. Supporting methods that employ either DFT or the data calculated using DFT offer valuable auxiliary information. This chapter presents an overview of the computational methods employed in calculating the results presented in Chapter 3.

2.1 Interaction of electrons and matter

The atomic-level description of a a system of electrons and nuclei starts from the time-independent Schrödinger equation

$$\mathcal{H}\Psi(\boldsymbol{r}) = E\Psi(\boldsymbol{r}), \tag{2.1}$$

where $\mathcal{H}$ is the Hamiltonian, $\Psi(\boldsymbol{r})$ is the wavefunction, and E is the eigenvalue of the Hamiltonian, i.e. the total energy of the system. The Hamiltonian can be expressed as

$$\begin{aligned}\mathcal{H} = &-\frac{\hbar^2}{2m_\mathrm{e}}\sum_i \nabla_i^2 - \sum_{i,I}\frac{Z_I e^2}{|\boldsymbol{r}_i - \boldsymbol{R}_I|} + \frac{1}{2}\sum_{i\neq j}\frac{e^2}{|\boldsymbol{r}_i - \boldsymbol{r}_j|} \\ &+ \frac{1}{2}\sum_{I\neq J}\frac{Z_I Z_J e^2}{|\boldsymbol{R}_I - \boldsymbol{R}_J|} - \frac{\hbar^2}{2M_I}\sum_I \nabla_I^2.\end{aligned} \tag{2.2}$$

The first term on the right hand side is the kinetic energy of the electrons. The second, third, and fourth terms are the Coulomb interactions between

the electrons and the nuclei, and the last term is the kinetic energy of the nuclei. Since the nuclei are significantly more massive than the electrons (the mass of a proton or a neutron is more than 1800 times the mass of an electron), the electrons can be considered to respond immediately to changes in the external potential caused by the movement of the nuclei. The kinetic energy of the nuclei can therefore be omitted from the Hamiltonian, and the nuclear coordinates can be regarded as parameters, rather than variables of the Hamiltonian. This separation of the movements of the electrons and nuclei is termed the adiabatic, or Born-Oppenheimer approximation, and is widely used in calculations.

2.1.1 Density functional theory

The foundations of the DFT are the Hohenberg-Kohn theorems, which can be stated as [5]
1. *The ground state particle density $n_0(\boldsymbol{r})$ of a system of interacting particles in an external potential $V_{\text{ext}}(\boldsymbol{r})$ uniquely determines the potential.*
2. *For the potential $V_{\text{ext}}(\boldsymbol{r})$, the exact ground state energy of the system is the global minimum of the functional $E[n]$, and the corresponding density is the exact ground state density $n_0(\boldsymbol{r})$.*

In principle, the ground state density determines all the properties of the system, although some of them can be practically inaccessible. The Hohenberg-Kohn approach simplifies the solution of the Schrödinger equation, because the density is a function of three position variables instead of the $3N$ variables of the many-body wavefunction (ignoring spin).

The analytic solution of the many-body Schrödinger equation is still possible only in very simple cases. A successful approach for the solution was proposed by Kohn & Sham [6], which assumes that the original interacting system can be replaced by a non-interacting system that yields the same ground state density. The resulting system of independent-particle equations can be considered soluble. The many-body effects are grouped into an exchange-correlation functional of the density. The solution of the Kohn-Sham system is an approximation of the solution of the original system, and the accuracy is limited by the exchange-correlation functional, for which no exact formulation is known.

The Kohn-Sham independent-particle equations in atomic units ($\hbar = 1$, $m_{\text{e}} = 1$, $e = 1$, $4\pi\varepsilon_0 = 1$) are

$$\left[-\frac{1}{2}\nabla^2 + V_{\text{KS}}(\boldsymbol{r})\right]\psi_i(\boldsymbol{r}) = \varepsilon_i\psi_i(\boldsymbol{r}), \tag{2.3}$$

where the effective potential $V_{\text{KS}}(\boldsymbol{r})$ is

$$V_{\text{KS}}(\boldsymbol{r}) = V_{\text{ext}} + V_{\text{H}} + V_{\text{xc}}. \tag{2.4}$$

and the independent-particle states satisfy

$$\sum_i |\psi_i(\boldsymbol{r})|^2 = n(\boldsymbol{r}). \tag{2.5}$$

The external potential V_{ext} is due to the interaction of the electrons with the nuclei, and the Hartree potential

$$V_{\text{H}} = \int \frac{n(\boldsymbol{r}')}{|\boldsymbol{r} - \boldsymbol{r}'|} \mathrm{d}^3\boldsymbol{r}' \tag{2.6}$$

corresponds to the electrostatic potential of the electrons. The exchange-correlation potential V_{xc} includes the many-electron effects. If the exact form of the exchange-correlation potential was known, the Kohn-Sham equations would yield the exact ground-state density and energy of the original, interacting system. The quality of the results is therefore determined by a large extent by the quality of the description of the exchange-correlation effects.

The simplest approximation to the exchange-correlation effects is the local density approximation (LDA) [6], in which the exchange-correlation energy density is taken to equal the value in a homogeneous electron gas with the same density. The exchange-correlation effects in solids are relatively short-ranged, and the LDA is successful in describing the bulk phase of metals where the valence electrons are nearly free. However, the LDA typically overestimates binding energies and underestimates bond lengths.

An improvement over the LDA are the family of exchange-correlation functionals based on the generalized gradient approximation (GGA) [11], which in addition to the density, depend on the gradient of the density. A still more refined family are the meta-GGAs, that depend also on the Laplacian (second derivative) of the density. Hybrid functionals mix exact exchange from Hartree-Fock theory to LDA or GGA. Depending on the functional, the amount of exact exchange is taken as a predetermined constant or determined by fitting to experimental data. The computational cost involved with the calculation of the exact exchange part practically limits the use of hybrid functionals to individual molecules.

The Kohn-Sham one-particle states $\psi_i(\boldsymbol{r})$ determine the density according to Eq. 2.5, and the density determines the effective potential. The solution must therefore be searched in a self-consistent manner, by first constructing an initial guess for the density. The effective potential can then be determined, and the solution of the Kohn-Sham equations gives a new density. The previous density is mixed with the new one, and the calculation is repeated until self-consistency is achieved, i.e. repeating the calculation does not change the density.

Typically, the core electrons are unaffected by the environment where an atom is located. The core states can be kept fixed, and the Kohn-Sham equations are only needed to be solved for the valence electrons. However, the

division to core and valence electrons is not unambiguous, and is dependent on the constituent atoms of the system in consideration. This frozen-core approximation is commonly implemented in computational procedures.

In practice, the wavefunctions $\psi_i(\boldsymbol{r})$ are represented as linear combinations of basis functions. Popular choices for basis functions are roughly divided into localized, atom-centered (e.g. Gaussian) functions, and plane waves. The localized basis sets are widely used for isolated molecules, whereas plane waves are particularly well suited for periodic systems because they obey the Bloch theorem, and plane waves are eigenfunctions of the momentum operator [1]. The ability of the basis to reproduce the wavefunction is determined by the number of plane waves included in the basis, and this parameter is controlled by the cutoff energy for a given unit cell size. The cutoff energy is the maximum kinetic energy associated plane waves in the basis:

$$E_{\text{cut}} = \frac{\hbar^2}{2m} G_{\text{cut}}^2, \tag{2.7}$$

where G_{cut} is the reciprocal lattice vector corresponding to the plane wave with kinetic energy E_{cut}.

Generally, plane wave basis implies periodic boundary conditions on the system. Isolated molecules need a large unit cell to avoid interactions between the periodic images, and the number of plane waves increases with cell size. Similar consideration has to be taken into account in surface calculations, where the surface is typically modeled using the repeated slab approach (see Fig. 2.1). The surface is constructed as a slab of several atomic layers with vacuum between the periodic images in the direction perpendicular to the surface to minimize interaction between the periodic images.

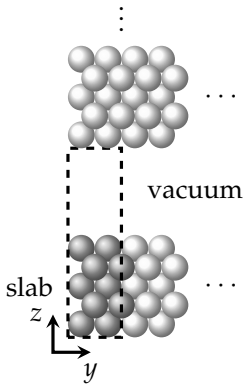

Figure 2.1: Repeated slab geometry of a fcc(100) surface. The surface is modeled by five atomic layers and a $p(2 \times 2)$ surface unit cell. The dark gray spheres are atoms in the unit cell, and the light gray spheres are their periodic images. The dashed line marks the limits of the unit cell.

Another complication that arises from the use of plane wave basis is the large cutoff energy needed to reproduce the rapid oscillations that the valence states exhibit near the nuclei due to the requirement of orthogonality with the core states [12].

The basis set size can be reduced while retaining accuracy by replacing the oscillatory part by a smooth function. The idea is employed in pseudopotential methods, but most of them do not preserve the all-electron wavefunction.

In the projector augmented wave (PAW) method [13], a smooth part $\tilde{\psi}_n$ of the valence wavefunction is defined inside atom-centered augmentation spheres. The smooth functions are related to the all-electron wavefunctions $|\psi_n\rangle$ via a linear transformation

$$|\psi_n\rangle = \mathcal{T}\,|\tilde{\psi}_n\rangle\,, \tag{2.8}$$

where $\mathcal{T}$ is an operator defined by

$$\mathcal{T} = \mathbf{1} + \sum_R \mathcal{T}^R, \tag{2.9}$$

where $\mathcal{T}^R$ acts only within the augmentation spheres. Inside the spheres, a basis of partial waves $|\varphi_i\rangle$ is defined, and again the operator $\mathcal{T}$ relates them to smooth partial waves $|\tilde{\varphi}_i\rangle$ by

$$|\varphi_i\rangle = (\mathbf{1} + \mathcal{T}^R)\,|\tilde{\varphi}_i\rangle\,. \tag{2.10}$$

The operator $\mathcal{T}^R$ only acts within the spheres, so $|\varphi_i\rangle = |\tilde{\varphi}_i\rangle$ outside the spheres. The smooth wavefunctions can now be expanded in the basis of the smooth partial waves as

$$|\tilde{\psi}_n\rangle = \sum_i c^R_{ni}\,|\tilde{\varphi}^R_i\rangle\,, \tag{2.11}$$

which also relates the functions outside the spheres with the same expansion coefficients c^R_{ni} since the smooth and full functions are related by the same linear transformation $\mathcal{T}$.

An orthogonal and complete set of smooth projector functions $|\tilde{p}^R_i\rangle$ are chosen inside the augmentation spheres:

$$\langle \tilde{p}^R_i | \tilde{\varphi}^R_j \rangle = \delta_{ij} \tag{2.12}$$

$$\sum_i |\tilde{\varphi}^R_i\rangle\,\langle \tilde{p}^R_i| = \mathbf{1}. \tag{2.13}$$

The expansion coefficients c^R_{ni} are then given as

$$c^R_{ni} = \langle \tilde{p}^R_i | \tilde{\psi}_n \rangle\,, \tag{2.14}$$

and the smooth and the full wavefunctions are then defined in terms of the partial waves and the projector functions as

$$|\tilde{\psi}_n\rangle = \sum_i \langle \tilde{p}_i^R | \tilde{\psi}_n \rangle \, |\tilde{\varphi}_i^R\rangle \tag{2.15}$$

$$|\psi_n\rangle = \sum_i \langle \tilde{p}_i^R | \tilde{\psi}_n \rangle \, |\varphi_i^R\rangle \, . \tag{2.16}$$

The operator $\mathcal{T}$ is now defined in terms of the partial waves and the projector functions:

$$\mathcal{T} = \mathbf{1} + \sum_R \sum_i \left(|\varphi_i^R\rangle - |\tilde{\varphi}_i^R\rangle \right) \langle \tilde{p}_i^R | \, , \tag{2.17}$$

and the full wavefunction can be written as a sum of a smooth part and a sum over atoms of a term that contains the partial waves, projector functions, and the smooth wavefunction:

$$|\psi_n\rangle = |\tilde{\psi}_n\rangle + \sum_R \left(\sum_i |\varphi_i^R\rangle \, \langle \tilde{p}_i^R | \tilde{\psi}_n \rangle - \sum_i |\tilde{\varphi}_i^R\rangle \, \langle \tilde{p}_i^R | \tilde{\psi}_n \rangle \right) . \tag{2.18}$$

When the Kohn-Sham equations are cast into the PAW formalism, an efficient way of solving the many-electron Schrödinger equation that preserves the full Kohn-Sham one-electron wavefunctions is obtained.

The computational procedures described above are implemented in the Vienna ab-initio simulation package (VASP) [14–18], which is used to calculate all the DFT results presented in this thesis.

It should be noted that the DFT ground state corresponds to $T = 0\,\mathrm{K}$, whereas experiments are always performed at nonzero temperatures.

2.2 Bader analysis

Bond formation typically involves modification of the distribution of electrons around the atoms involved. This can lead to dipole formation and strong modification of the electronic properties of surfaces by adsorbates, for example changes in the work function. Differences in electronegativity lead to charge transfer between atoms. A prominent example of charge transfer are compounds with ionic bonding, where the more electronegative element receives electron density from the less electronegative one, becoming negatively charged.

The central quantity in DFT calculations, the electron density, naturally allows analysis of the electron distribution. However, it is not trivial how to assign electron density to belong to a certain nucleus. Bader analysis [19] is a method particulary suitable for DFT with planewave basis, since it does not require atom-centered basis functions.

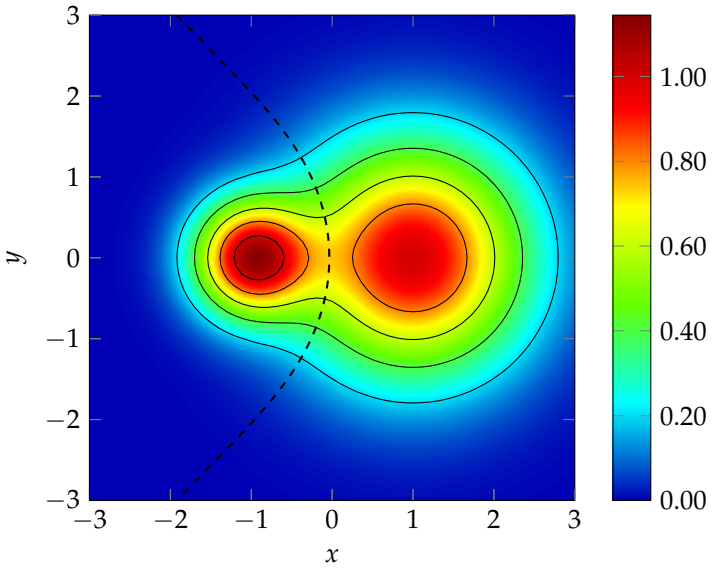

Figure 2.2: Example of the division of a 2D function to Bader areas. The function is a sum of Gaussian peaks centered at $(-1, 0)$ and $(1, 0)$ with $\sigma = 0.5$ and 1.0, respectively. The solid lines are contours at 0.2 to 1.0 with interval 0.2. The dashed line is the zero-flux line.

The main principle of Bader analysis is to find the zero-flux surfaces of the electron density between the nuclei. The zero-flux surfaces are described by

$$\nabla\rho(\boldsymbol{r}) \cdot \hat{\boldsymbol{n}}(\boldsymbol{r}) = 0, \tag{2.19}$$

that is, the zero-flux surfaces have no component of the electron density gradient in the direction $\hat{\boldsymbol{n}}$ normal to the surface. These surfaces divide the electron density into areas containing one electron density maximum each, and the total electron density enclosed by a zero-flux surface is associated with the atom bounded by the surface. The amount of electrons associated with the atoms are calculated by integrating the electron density within the Bader volumes. Comparing the number of electrons in the Bader volume to the number of electrons in an isolated atom gives the amount of electrons transferred.

Figure 2.2 shows the division of a two-dimensional 'density' into Bader areas. The function is a sum of two Gaussian peaks centered at $(-1, 0)$ and $(1, 0)$ with $\sigma = 0.5$ and 1.0, respectively.

2.3 Nudged elastic band method

An important class of problems in solid-state physics and theoretical chemistry is the estimation of transition probabilities from a stable atomic configuration to another, as in conformational changes in molecules, or diffusion in solids and at surfaces. An energetically likely route for the process is the minimum energy path (MEP), along which least energy has to be supplied to the system for the process to take place. The transition probability between the initial and final states is closely connected to the energy barrier along the MEP.

The nudged elastic band (NEB) method [20, 21] is a way of finding saddle points and MEPs between known initial and final states. A chain of intermediate configurations (images) are constructed between the initial and final states. The images feel a spring force along the reaction path, and the component of the true force perpendicular to the path. The spring force keeps the images equally separated along the path, and the true force component 'nudges' the images towards the MEP. While the images can be optimized in parallel, they are not completely independent of each other, since the coordinates of neighboring images are needed to evaluate the local path tangent direction at an image to project out the perpendicular component of the spring force and the parallel component of the true force. Once converged, the images lie on the MEP.

The NEB method does not guarantee finding the energy barrier along the MEP, due to the spring forces keeping the images equidistant. Increasing the number of images improves the estimate, but none of the images is converged to the maximum energy along the MEP. A modification of the NEB method that converges an image to the maximum energy is the climbing image nudged elastic band (CINEB) method [22]. The image with the highest energy does not feel the spring force, and instead of minimizing the energy as for the other images, its energy along the path is maximized. The image is driven to the maximum energy along the MEP. The CINEB method therefore finds a good estimate for the energy barrier with a reasonable number of images. In practice however, it may be necessary to perform a standard NEB calculation to preconverge images before switching to the CINEB method.

2.4 Vibrational frequency analysis

The vibrational spectrum of adsorbates on surfaces are readily accessible in experiments. The vibrational frequencies of adsorbed molecules can give information about the adsorption site and surface coordination of the molecule. Vibrational analysis serves as an important tool for validation of DFT results since the calculated frequencies can be directly compared to experimental results.

The calculation of vibrations of an adsorbate on a surface begins from the relaxed geometry with the adsorbate in an equilibrium position in an energy minimum, such that small displacements from the equilibrium position direct the atom back towards equilibrium. Within the harmonic approximation, the vibration frequencies are calculated from the forces acting on the nuclei [23]. The atoms are displaced by a small amount δ towards the positive and negative direction along each cartesian axis (see Fig. 2.3), and the force constants Φ_{ij} are the second derivatives of energy with respect to position:

$$\Phi_{ij} = \frac{\partial^2 E}{\partial r_i \partial r_j} = \frac{F_{ij}^{+} - F_{ij}^{-}}{2\delta}. \tag{2.20}$$

The displacement δ must be small enough for the forces to remain in the linear regime.

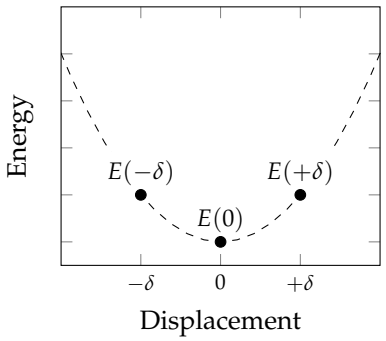

Figure 2.3: To determine vibrational frequencies, an atom is displaced from the equilibrium position by $\pm\delta$. The energies of the displaced configurations are used to calculate the force constants in the harmonic approximation.

If the configuration of atoms is a saddle point of energy, the second derivative of energy has a negative sign in a certain direction. The configuration is in this case unstable to small distortions, which is indicated by imaginary values of vibrational frequencies of the vibrational modes corresponding to displacements driving the structure downhill in the potential energy landscape.

2.5 Work function

The energy required to remove an electron from a surface, the work function, is an important quantity in e.g. electron guns, where thermal energy causes electrons to detach from the surface, and in photoelectric devices, where the electrons are detached by photons. It can be measured experimentally via thermionic emission, photoemission, field electron emission, electron tunnelling, or contact potentials.

The work function is given as

$$\phi = -U - \varepsilon_{\mathrm{F}}, \tag{2.21}$$

where U is the saturation level of the potential outside the surface, and ε_{F} is the Fermi level. Since the work function depends on the properties of the surface, different crystal faces of the same material have different work functions in general [24].

Figure 2.4 shows the procedure to determine the work function of a surface from DFT calculations. The local electrostatic potential is averaged in the z-direction. The work function is the potential difference from the Fermi level to the potential outside the surface, where the potential is flat. Note the small change in the potential in Fig. 2.4 at $z = 32$ Å, which is caused by dipole corrections added to the potential to account for the inequal geometries at the different sides of the slab. The top layers are allowed to relax while the bottom layers are held fixed at the bulk lattice constant, and the potential outside the relaxed and unrelaxed surfaces are not equal. Because of the periodicity of the system, the potential would have a slope in the vacuum region if the dipole corrections would not be included. The potential would not become flat and the work function could not be determined unambiguously. Here the effect is small, but for adsorption systems where the adsorbates strongly modify the potential, the dipole corrections become important.

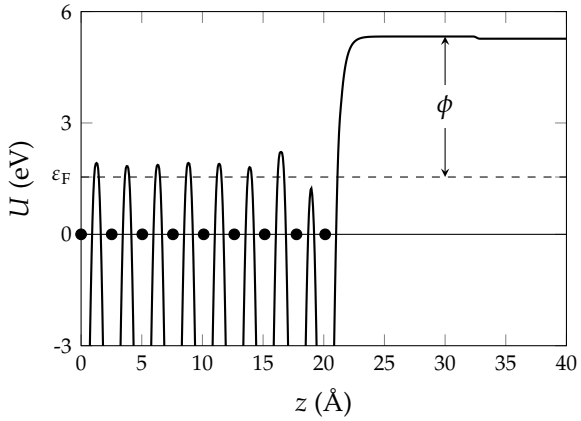

Figure 2.4: Local potential of a Pb(100) surface averaged in the z-direction. The dashed line marks the Fermi level. The black dots indicate the position of the Pb layers.

2.6 Lattice constant

To avoid lattice stress is calculations, the equilibrium lattice constant is needed. The lattice constants obtained by DFT-GGA usually differ from the experimental values by less than 2 % [25].

When changing the lattice constant, the equilibrium lattice constant yields minimum energy. The minimum is obtained by fitting an equation of state (EOS) to the calculated (V, E) data. Popular EOSs are the Murnaghan EOS [26] and the Birch-Murnaghan EOS [27], that give reasonable results for the purpose of finding the equilibrium lattice constant with reasonably small deviations from the equilibrium. In addition, these EOSs allow the determination of the bulk modulus. However, direct comparison with experimental bulk modulus might not be possible due to the DFT results corresponding to $T = 0\,\mathrm{K}$ whereas the experimental values are often determined at room temperature, and if zero-point effects are ignored in the DFT calculation [28].

The Murnaghan EOS is given by

$$E(V) = E_0 + \frac{B_0 V}{B_0'}\left[\frac{\left(\frac{V_0}{V}\right)^{B_0'}}{B_0' - 1} + 1\right] - \frac{B_0 V_0}{B_0' - 1} \tag{2.22}$$

and the Birch-Murnaghan EOS by

$$E(V) = E_0 + \frac{9 V_0 B_0}{16}\left\{\left[\left(\frac{V_0}{V}\right)^{\frac{2}{3}} - 1\right]^3 B_0' + \left[\left(\frac{V_0}{V}\right)^{\frac{2}{3}} - 1\right]^2 \left[6 - 4\left(\frac{V_0}{V}\right)^{\frac{2}{3}}\right]\right\}, \tag{2.23}$$

where V_0 is the equilibrium volume of the cell, E_0 is the energy at the equilibrium volume, and B_0 and B_0' are the bulk modulus and the pressure derivative of the bulk modulus at equilibrium volume, respectively. Figure 2.5 shows comparison of Eqs. (2.22) and (2.23) for $B_0 = 173\,\mathrm{GPa}$ and $B_0' = 6.29$. In the scale of the plot, the two curves are nearly indistinguishable, except at the extremes. Typically, the lattice constants calculated with Eqs. (2.22) and (2.23) agree within 10^{-3} Å and the bulk moduli within a few percent, if the deviations from the equilibrium volume are reasonably small.

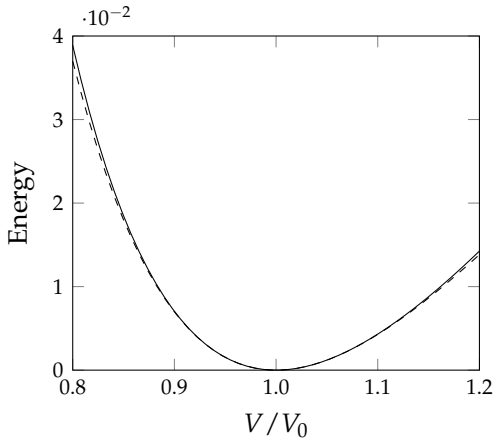

Figure 2.5: Comparison of the Murnaghan EOS (solid line) and the Birch-Murnaghan EOS (dashed line). The bulk modulus and its pressure derivative are the tabulated values for gold.

CHAPTER 3

Review of the computational results

The thesis includes three publications that cover distinct surface phenomena. Publication I deals with molecular oxygen adsorption on the Ag(110) surface. Publications II and III include processes on the Pb(100) surface, namely potassium and oxygen adsorption.

3.1 Oxygen adsorption on Ag(110)

The catalytic importance of the interactions of silver and oxygen is manifested by numerous industrial applications, e.g. oxidative dehydrogenation of methanol to formaldehyde [29], photolysis of molecular oxygen [30], and epoxidation of ethylene [31, 32]. Silver-based catalysts are also employed in several 'green chemistry' processes [33].

Although the O/Ag(110)-system has been studied extensively both theoretically and experimentally, some controversies were still present. These include the preferred orientation of the adsorbed O_2 molecule on the Ag(110) surface, the effects that promote the O_2 dissociation, and the diffusion of oxygen atoms after the dissociation of the molecule. Publication I clarifies these points and provides a detailed vibrational analysis of atomic and molecular oxygen on Ag(110). Our results indicate, contrary to some previous theoretical studies [34, 35] and in accordance with others [36, 37], that the preferred adsorption orientation of O_2 on Ag(110) is such that the molecular axis is aligned in the $[1\bar{1}0]$ direction. The results also suggest that after dissociation of the O_2 molecule, the oxygen atoms occupy threefold hollow sites rather than short bridge sites, as suggested by an experimental study [38]. The dissociation is coupled with a surface phonon mode that facilitates the dissociation in the $[001]$ direction. A recent study has shown that O_2 adsorption on Ag(110) leads to surface roughening which is expected to increase the catalytic activity of the surface [39].

An angle-resolved photoemission study [40] has reported three modes of oxygen adsorption on Ag(110): physisorbed O_2 at $T < 40\,\mathrm{K}$, chemisorbed O_2 at 60 K to 180 K, and chemisorbed O (dissociated) at $T > 180\,\mathrm{K}$. The (110) surface of a face-centered cubic (fcc) lattice has five possible oxygen

adsorption sites: fourfold hollow (FFH), threefold hollow (TFH), top (TP), long bridge (LB), and short bridge (SB). The sites are shown in Fig. 3.1.

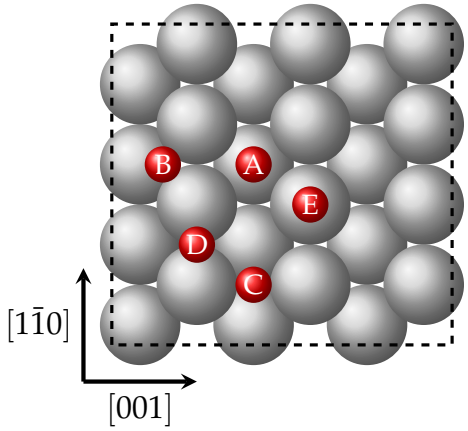

Figure 3.1: Oxygen adsorption sites on the fcc(110) surface. The sites are labeled A: fourfold hollow, B: threefold hollow, C: long bridge, D: short bridge, and E: top. The dashed lines limit the (3×4) unit cell used in this study.

3.1.1 Adsorption and dissociation of O_2

Our spin-polarized DFT calculations were performed using VASP with the Perdew, Burke, and Ernzerhof (PBE) exchange-correlation functional. The Ag(110) surface is modeled by a five-layer slab of (3×4) cell and 10 Å vacuum in the z direction. The cutoff energy was set to 500 eV. Bulk calculations give Ag lattice constant of 4.147 Å (see Fig. 3.2), in good agreement with the experimental value, 4.086 Å.

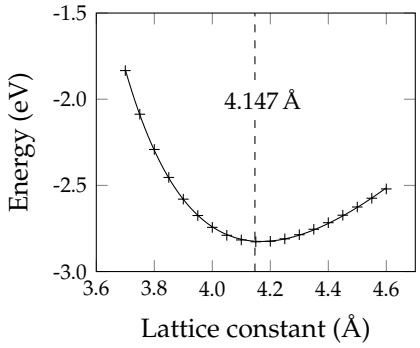

Figure 3.2: Equilibrium lattice constant of silver. Murnaghan equation of state is fitted to calculated (a, E)-data points.

The previously published studies agree in that the O_2 adsorbed on Ag(110) lies flat on a FFH site, but the preferred molecular orientation has been controversial. According to Gravil & Bird, O_2 molecular axis orientation in the $[001]$ direction is preferred to the $[1\bar{1}0]$ direction by 40 meV [34], while Olsson et al. found the $[001]$ and $[1\bar{1}0]$ orientations to have the same adsorption energy [35]. Van den Hoek & Baerends report $[1\bar{1}0]$ orientation to be preferred on an Ag cluster [36], and Monturet et al. found $[1\bar{1}0]$ orientation to be preferred by a margin of 10 meV [37].

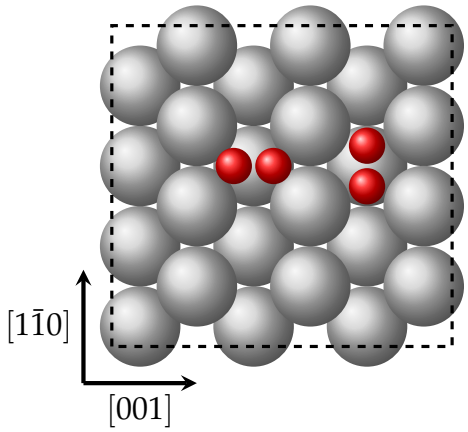

Figure 3.3: Oxygen molecule adsorption orientations on the fourfold hollow site on the fcc(110) surface. The O_2 molecule on the left is oriented in the $[001]$ direction ($O_2[001]$). The O_2 molecule on the right is oriented in the $[1\bar{1}0]$ direction ($O_2[1\bar{1}0]$).

The energy difference of the orientations is small, and both orientations are likely to coexist on the Ag(110) surface, as is reported in an experimental study by Hahn & Ho. Their scanning tunnelling microscopy (STM) results indicate the ratio of $O_2[1\bar{1}0]$ to $O_2[001]$ to be 1.41 at 45 K and 1.35 at 75 K. This suggests that the $[1\bar{1}0]$ orientation would be energetically preferred to the $[001]$ orientation.

Our results confirm the FFH site to be the energetically preferred adsorption site, and the $[1\bar{1}0]$ is the preferred orientation (see Table 3.1) by 40 meV compared to the $[001]$ orientation. The TP site is unstable in both orientations, and the short bridge siter is marginally stable in the $[1\bar{1}0]$ direction and unstable in the $[001]$ direction. The opposite holds for the long bridge site.

The O_2 molecule gains electrons from the substrate at all adsorptions sites and orientations, and the bond length of the oxygen molecule is elongated. The electrons transferred to the adsorbed O_2 molecule occupy the antibonding $2\pi^*$ orbital, which leads to weakening of the O-O bond that facilitates the dissociation of the molecule.

The electron density difference in a vertical plane along the O-O bond for O_2 adsorbed on the FFH site aligned in the $[1\bar{1}0]$ and $[001]$ directions is shown in Fig. 3.4. In both orientations, electron depletion occurs in between the oxygen atoms, characteristic of weakening of the O-O bond. Electron accumulation occurs between oxygen and silver atoms, indicating O-Ag bond formation.

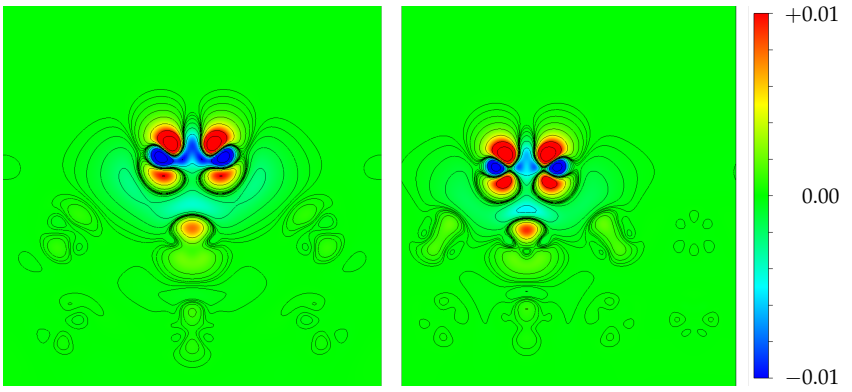

Figure 3.4: Electron density difference of O_2 adsorbed on the FFH site. (a) O_2 aligned in the $[1\bar{1}0]$ direction. (b) O_2 aligned in the $[001]$ direction. Red and blue areas indicate electron accumulation and depletion, respectively.

Table 3.1: Adsorption energy, bond length, and charge transfer of the O_2 molecule on the Ag(110) surface with molecular axis oriented in the $[001]$ and $[1\bar{1}0]$ directions. The adsorption sites are labeled FFH (fourfold hollow), TP (top), SB (short bridge), and LB (long bridge).

Adsorption site	O_2 orientation	Adsorption energy (eV)	d_{O-O} (Å)	Charge transfer to O_2 (electrons)
FFH	$[001]$	0.37	1.428	0.90
	$[1\bar{1}0]$	0.41	1.465	0.95
TP	$[001]$	−0.45	1.328	0.54
	$[1\bar{1}0]$	−0.42	1.329	0.55
SB	$[001]$	−0.12	1.412	0.81
	$[1\bar{1}0]$	0.07	1.341	0.71
LB	$[001]$	0.07	1.334	0.64
	$[1\bar{1}0]$	−0.07	1.470	0.98

CINEB calculations show that the O_2 dissociation barriers for $O_2[1\bar{1}0]$ and $O_2[001]$ are 0.50 eV and 0.42 eV, respectively. The values are more than 0.1 eV lower than values reported previously [34] by Gravil et al. The dissociation is more facile in the $[001]$ direction, which has also been reported in the case of Rh(110) [41] and Cu(110) [42] surfaces.

In the dissociation of $O_2[001]$, the silver atoms in the top layer are displaced away from the oxygen atoms in the $[001]$ direction and the second layer Ag atoms move upwards. This displacement pattern matches a surface Rayleigh phonon mode whose frequency is found to be 4.0 meV (5.0 meV in experiments [43, 44] and 4.2 meV to 4.4 meV in other theoretical calculations [45–47]). The more facile dissociation of $O_2[001]$ compared to $O_2[1\bar{1}0]$ on Ag(110) is therefore linked to the coupling of the molecular stretching to surface vibrations.

3.1.2 Adsorption and diffusion of atomic oxygen

The adsorption energies of atomic oxygen are given in Table 3.2. The energies on the FFH and TFH sites are almost equal (3.88 eV and 3.87 eV, respectively). The adsorption energy on the LB site (3.81 eV) is also rather close to the values for the FFH and TFH sites, while the SB site has 3.48 eV. It is thus likely that the FFH, TFH, and LB sites are occupied almost equally at higher oxygen coverages.

Bader analysis shows that the charge transfer follows the coordination number so that sites with higher coordination have more electrons transferred to oxygen. Electron density difference plots along the Ag-O bonds for O adsorbed on the FFH and TFH sites (Fig. 3.5) show the charge accumulation around the oxygen atom.

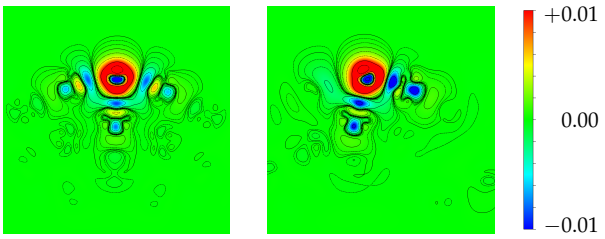

Figure 3.5: Electron density difference for (a) oxygen atom on a FFH site and (b) oxygen atom on a TFH site. The slices are oriented along Ag-O bonds.

The density of states (DOS) projected to the *p*-states of oxygen adsorbed on the FFH and TFH sites and the *d*-states of the silver (110) surface are presented in Fig. 3.6. Hybridization of the oxygen *p*-states with the silver *d*-states induces a small peak in the Ag DOS just below the Fermi level. Such states are missing in the DOS of the clean Ag(110) surface. Since the DOS near the Fermi level is linked to the reactivity of a surface, the adsorbed oxygen species are likely to enhance the reactivity of the Ag(110) surface.

CINEB calculations of show that oxygen atom diffusion from an SB site to a TFH site in the $[001]$ direction experiences no energy barrier. The diffusion

Table 3.2: Adsorption energy (referenced to the free oxygen atom), coordination number, Ag-O bond length, and charge transfer of atomic oxygen on the Ag(110). The adsorption sites are labeled FFH (fourfold hollow), TFH (threefold hollow), SB (short bridge), and LB (long bridge). The bond lengths in italics represent the O-Ag bond lengths to Ag atoms in the second layer.

Ads. site	Ads. energy (eV)	Coordination number	$d_{\text{Ag-O}}$ (Å)		Charge transfer (electrons)
FFH	3.88	5	2.396	*2.285*	0.93
TFH	3.87	3	2.147	*2.223*	0.88
SB	3.81	4	2.312	*2.203*	0.91
LB	3.48	2	2.038	(—)	0.81

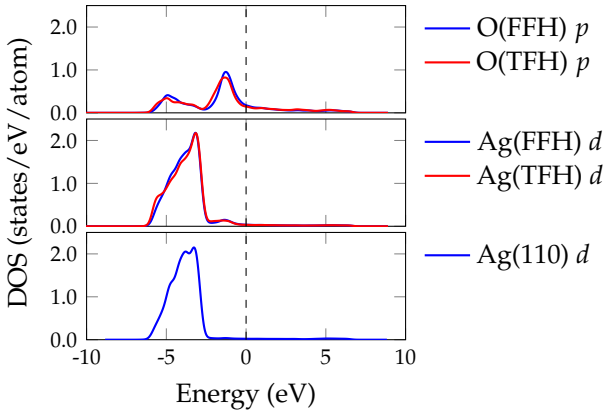

Figure 3.6: Projected DOS on the p states of oxygen adsorbed on Ag(110) (top), on the d states of Ag atoms bonded to oxygen (middle), and on the d states of clean Ag(110) surface (bottom).

from TFH to FFH has a very small barrier of 30 meV. With no barrier, the oxygen atom can diffuse spontaneously from an SB site to TFH in the presence of even a small perturbation. The diffusion from an SB to another SB in the [001] direction through a FFH site experiences a barrier of 420 meV. Diffusion from a FFH site to another FFH site along the Ag rows in the $[1\bar{1}0]$ direction has a small barrier of 72 meV. This path includes a local minimum at the LB site, and the barrier from LB to FFH is 45 meV. The preferred direction of oxygen atom diffusion from a FFH site to another FFH site is therefore the $[1\bar{1}0]$ direction owing to the significantly lower diffusion barrier in that direction (72 meV) compared to the [001] direction (420 meV).

Our results lead to different conclusions than is reported by Hahn & Ho [38]. They report oxygen atom diffusion from an SB site to another SB site, and that diffusion between SB sites is easier than from an SB site to a FFH site.

Our results indicate that oxygen binding energy is 0.39 eV lower on the TFH site than on the SB site, and the diffusion pathway from SB to TFH has no energy barrier. In addition, the SB and TFH sites are separated by just 1.265 Å, which makes it difficult to differentiate between these sites in interpreting STM images. We believe the oxygen species reported by Hahn & Ho as occupying the SB sites are mainly occupying the TFH sites.

3.1.3 Vibration of atomic and molecular oxygen on Ag(110)

The vibrational analysis was performed using the finite difference method implemented in VASP. The vibration frequencies of atomic oxygen were calculated at four different adsorption sites. The values for the frequencies of O-Ag stretching and frustrated translation along the $[001]$ and $[1\bar{1}0]$ directions are presented in Table 3.3.

Table 3.3: Atomic oxygen vibration frequencies on Ag(110).

Vibration mode Vibration mode	FFH (meV)	TFH (meV)	SB (meV)	LB (meV)
O-Ag stretch	38	44	54	43
Frustrated translation, $[1\bar{1}0]$	21	41	51	35
Frustrated translation, $[001]$	20	33	-10	22

Experimental vibration frequencies obtained by electron energy loss spectroscopy (EELS) measurements report values of 40.5 meV [48], 39.1 meV [49], and 40.0 meV [50] for the O-Ag stretching mode. These studies do not report the site on which the oxygen atoms are located, but the experimental values are closer to the calculated value for the FFH site than for other sites.

The negative vibration frequency of oxygen on SB for frustrated translation in the $[001]$ direction further consolidates the view that the SB site is unstable at the coverage considered here. The vibration mode directs the oxygen atom towards the TFH site, and since the diffusion pathway from SB to TFH is barrierless, it is unlikely that oxygen would occupy the SB site.

Our calculations find vibration frequency of 194 meV for the free O_2 molecule, which is in good agreement with the experimental value (196 meV). As the molecule is adsorbed on the Ag(110) surface, the intramolecular interactions are modified and the interactions with the surface give rise to new modes of vibration. The highest frequency mode of the adsorbed molecule on all four sites and both orientations considered is the O-O stretching mode. The O-O stretching mode vibration frequency of the O_2 molecule adsorbed on the FFH site and oriented in the $[1\bar{1}0]$ direction is the same for calculations where the substrate is allowed to vibrate, and for calculations where the substrate is kept frozen. However, for O_2 oriented in the $[001]$ direction on the FFH site, the vibration frequency in the frozen substrate case is 12 meV lower than in the unfrozen case. This suggests that

the O_2 vibration couples to the substrate vibration only when adsorbed in the $[001]$ direction, which helps to explain why the O_2 dissociation barrier is lower for O_2 aligned in the $[001]$ direction than for O_2 aligned in the $[1\bar{1}0]$ direction.

3.2 Potassium adsorption on Pb(100)

Alkali metal adsorption is a seemingly simple process due to the electronic structure of the alkali atoms. Alkalis have closed inner shells and a single electron in the outer s shell. Therefore, alkalis on metal surfaces were used as model systems in developing an understanding of adsorption on metal surfaces in general [51–57].

The simplicity of the alkali adsorption systems was challenged by density functional theory studies and experiments in the early 1990s [58, 59]. A closer look at alkali adsorption revealed several complications, such as low-coordination adsorption sites [59, 60], substitutional adsorption [58–60], coverage-dependent adsorption site preference [61], island formation [62], and surface alloying [63]. Alkali adsorbates are known to affect the reactivity of surfaces by modification of the surface electronic structure [64].

Previous experimental studies on potassium adsorption on the low-index surfaces of lead have found surface reconstructions on Pb(110) [65] and Pb(111) [66] induced by adsorption at room temperature. An earlier study of potassium adsorption on the Pb(110) surface found no reconstruction for adsorption at 200 K [67]. On the Pb(111) surface, the reported $(\sqrt{3} \times \sqrt{3})\mathrm{R}30^\circ$ structure is not formed for adsorption at temperatures below 200 K. This suggests that the surface structure formation of these systems is temperature activated.

Publication II presents an experimental and density functional theory study of potassium adsorption on the (100) surface of lead. The results suggest that substitutional adsorption is preferred, and that the stable structure at submonolayer coverages is the $c(2 \times 2)$ structure.

3.2.1 Density functional theory calculations

The DFT calculations were performed using VASP and the PBE exchange-correlation functional. We have used cutoff energy of 350 eV. The calculated bulk lattice constant of lead, 5.046 Å (see Fig. 3.7), is within 2 % of the experimental value (4.95 Å). The Pb(100) surface is modeled by a seven layer slab with approximately 20 Å vacuum between the periodic images in the z-direction. Two of the bottom layers are frozen to the bulk lattice constant.

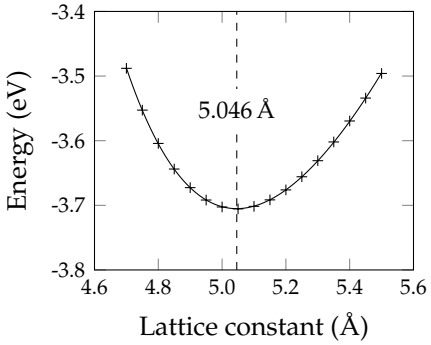

Figure 3.7: Equilibrium lattice constant of lead. Murnaghan equation of state is fitted to calculated (a, E)-data points.

The adsorption energy of potassium was calculated at four different adsorption sites at coverages $\Theta = 0.11$, 0.25, 0.50, and 1.00 monolayers (ML). The definition of monolayer coverage used here refers to one adsorbate particle for each substrate atom of a clean substrate surface. The structure models were $p(3 \times 3)$, $p(2 \times 2)$, $c(2 \times 2)$, and $p(1 \times 1)$, respectively. The energies are given in Table 3.4. The adsorption energy for on-surface adsorption is defined as

$$E_{\text{ads}} = -\frac{1}{N}\left(E_{\text{K/Pb(100)}} - E_{\text{Pb(100)}} - NE_{\text{K}}\right), \tag{3.1}$$

where N is the number of potassium atoms in the unit cell, $E_{\text{K/Pb(100)}}$ is the total energy of the K/Pb(100) system, $E_{\text{Pb(100)}}$ is the total energy of the Pb(100) slab, and E_{K} is the energy of the potassium atom.

If the potassium atoms occupy substitutional sites, the lead atoms originally on those sites need to be displaced. The problem with DFT calculations is that this changes the number of Pb atoms in the unit cell, and the energy needed to remove them from the unit cell has to be taken into account. A straightforward way is to assume that the Pb atoms diffuse to step edges on the surface and rebind at kink sites. Adding an atom to a kink site is effectively the same as adding an atom in the bulk, as can be confirmed by simply identifying the bonding environments of atoms in such a system. The adsorption energy in the case of substitutional adsorption is therefore

$$E_{\text{ads, subst.}} = -\frac{1}{N}\left(E_{\text{K/Pb(100)}} - E_{\text{Pb(100)}} - NE_{\text{K}} + NE_{\text{Pb}}^{\text{bulk}}\right), \tag{3.2}$$

where $E_{\text{Pb}}^{\text{bulk}}$ is the bulk cohesive energy of a lead atom. With the choice of signs used here, positive adsorption energy denotes thermodynamically stable adsorption.

The bulk energy is calculated by the method described by Fiorentini & Methfessel [68]. For sufficiently thick slabs

$$E_{\text{slab}}^{N} \approx 2\sigma + NE_{\text{bulk}}, \tag{3.3}$$

where E^N_{slab} is the energy of a N-layer slab, σ is the surface energy, and E_{bulk} is the energy of a bulk atom. Equation 3.3 represents a straight line with slope E_{bulk} in a (N, E^N_{slab}) coordinate system. The sufficient thickness for straight-line behaviour depends on the material in question, but typically the straight-line behaviour is seen for thin slabs of just a few (4–5) layers. This method has the advantage that the bulk energy can be determined using the same unit cell and k-point grid as is used for the surface calculations.

Table 3.4: Average potassium adsorption energy (in eV), work function change (in eV), and charge transferred from K to Pb (electrons) on a Pb(100) surface.

	hollow	bridge	ontop	subst.
$p(3\times3)\ \Theta = 0.11\,\text{ML}$				
E_{ads}	1.432	1.282	1.133	1.696
$\Delta_{\text{K-Pb1}}$	2.657	2.844	3.066	0.813
$\Delta\phi$	-1.329	-1.484	-1.644	-0.465
ΔQ	0.75	0.76	0.75	0.77
$p(2\times2)\ \Theta = 0.25\,\text{ML}$				
E_{ads}	1.286	1.095	0.957	1.695
$\Delta_{\text{K-Pb1}}$	2.570	2.815	3.021	0.977
$\Delta\phi$	-2.225	-2.318	-2.333	-0.992
ΔQ	0.69	0.67	0.65	0.75
$c(2\times2)\ \Theta = 0.50\,\text{ML}$				
E_{ads}	1.197	1.075	0.981	1.593
$\Delta_{\text{K-Pb1}}$	2.739	3.074	3.305	0.979
$\Delta\phi$	-1.672	-1.497	-1.467	-1.567
ΔQ	0.55	0.48	0.45	0.72
$p(1\times1)\ \Theta = 1.00\,\text{ML}$				
E_{ads}	0.891	0.771	0.678	—
$\Delta_{\text{K-Pb1}}$	2.862	3.258	3.588	—
$\Delta\phi$	-0.990	-0.975	-1.049	—
ΔQ	0.40	0.27	0.21	—

At coverage $\Theta = 0.11\,\text{ML}$, approximately 0.75 electrons are transferred from the potassium atoms to the substrate at all adsorption sites. For the hollow, bridge, and ontop sites, the adsorption energy decreases as a function of coverage. The charge transfer to substrate leaves the potassium atoms positively charged, and introduces a dipole moment that lowers the work function of the surface. The decrease in adsorption energy as a function of coverage can be understood as a consequence of the repulsive interaction between the dipoles that are located closer to each other. The repulsion is reduced by smaller charge transfer at higher coverages.

On the substitutional site, the adsorption energy is nearly constant (1.6 eV

to 1.7 eV) at coverages 0.11 ML to 0.50 ML, and also the charge transfer is reduced much less than on the on-surface sites as coverage is increased. The substitutional adsorption site allows the potassium atoms to sink closer to the level of the first lead layer, allowing the lead atoms to shield the repulsion between the adsorbate-induced dipoles. As a result, the substitutional site has the highest adsorption energy at higher coverages.

3.2.2 Comparison to LEED experiment

The only ordered K/Pb(100) adsorption structure observed in LEED experiments was a $c(2 \times 2)$ superlattice, with complete $c(2 \times 2)$ layer corresponding potassium coverage of $\Theta = 0.5$. The best-fit structure in LEED intensity analysis had the potassium atoms at substitutional sites.

The DFT results of interlayer separations, K-Pb bond length, and vibration frequency of potassium in the direction perpendicular to the surface of the $c(2 \times 2)$ structure with potassium atoms occupying substitutional sites are compared to values obtained by LEED analysis in Table 3.5.

Table 3.5: Computational and experimental structural parameters of potassium adsorbed on Pb(100) at substitutional sites in a $c(2 \times 2)$ structure. $\Delta_{\text{K-Pb1}}$ is the vertical spacing between the K layer and the first Pb layer (in Å), $d_{\text{K-Pb}}$ is the bond length between K and Pb (in Å), and $\Delta_{\text{Pb}ij}$ is the vertical separation between the ith and jth Pb layer (in Å). $E_{\text{K-Pb}}$ is the vibration energy of the K atoms (in meV).

Parameter	DFT	LEED
$\Delta_{\text{K-Pb1}}$	0.979	0.93 ± 0.02
$d_{\text{K-Pb}}$	3.70	3.62 ± 0.02
Δ_{Pb12}	2.110	2.07 ± 0.03
Δ_{Pb23}	2.572	2.56 ± 0.02
Δ_{Pb34}	2.507	2.41 ± 0.04
Δ_{Pb45}	2.519	2.49 ± 0.05
Δ_{Pb56}	2.606	2.45 ± 0.26
$E_{\text{K-Pb}}$	9.38	9.4 ± 0.5

Table 3.5 shows good agreement between the theoretical and experimental parameters. The DFT interlayer spacings and the K-Pb bond length are systematically slightly larger than the experimental values, which is partly explained by the overestimated bulk lattice constant in DFT (approximately 2 %). The vibrational frequency $E_{\text{K-Pb}}$ corresponds to the zone-center vibration energy of the K atoms, in the direction perpendicular to the surface. The calculated value is in excellent agreement with the experimental one.

3.3 Oxygen adsorption on Pb(100)

The largest amount of lead is used in lead-acid batteries, but the different colors of lead compounds have found use in pigments [69], and lead oxide has been shown to act as the active layer in a photovoltaic device [70]. The toxicity of lead severely restricts its use in products where it can get in contact with skin or get into the digestive or the respiratory system [69].

Lead oxidizes in several structures and typically exists in two oxidation states, II and IV. Common oxide structures include lead(II) oxide (PbO), lead(IV) oxide (PbO_2), and lead(II,IV) oxide (Pb_3O_4) (see Fig. 3.8). Lead(II) oxide (PbO), which is the commonly observed species on oxidized lead facets, exists in bulk form in two polymorphs; tetragonal α-PbO (litharge) and orthorhombic β-PbO (massicot). Litharge is stable at low temperatures, and controlled heating and cooling can be used to change the structure of PbO between the two polymorphs [71].

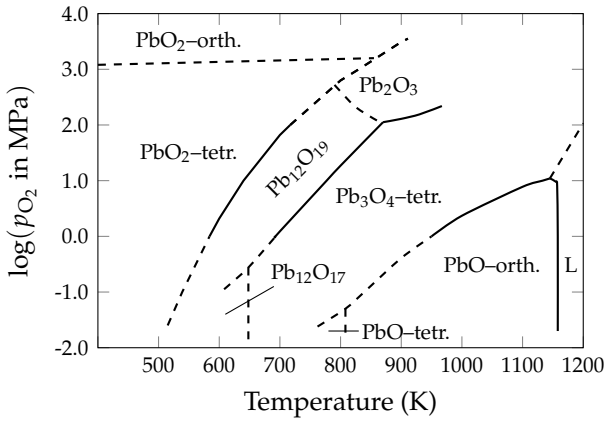

Figure 3.8: Pressure-temperature phase diagram of lead-oxygen compounds. After [72].

Our DFT results of binding energy, work function and charge transfer at coverages 0.06 ML to 1.00 ML suggest that the stable oxide structure formed on Pb(100) is a massicot-like two-layer structure where the oxygen atoms occupy distorted hollow sites.

3.3.1 Trends in binding energy, work function and charge transfer

Adsorption was considered on the Pb(100) surface at hollow, bridge, on-top, and a distorted hollow (labeled hollow2) sites, and subsurface adsorption on the sub-bridge and sub-hollow sites. Structural parameters, oxygen binding energies, work function, and charge transfer were calculated at a

coverage range of 0.06 ML to 1.00 ML, and the properties of a stable surface oxide layer at 2 ML coverage were analyzed.

The Pb(100) surface was modeled by a slab of 9 layers, with the bottom four layers frozen to the bulk positions. The calculated bulk lattice constant of lead was 5.046 Å. The periodic images had approximately 24 Å of vacuum between them in the z-direction.

The trends in the calculated quantities (Fig. 3.9) differ among the adsorption sites. The binding energy of oxygen decreases on the ontop and bridge sites, but increases on the hollow and hollow2 sites. The work function increases on the ontop and bridge sites, and decreases on the hollow and hollow2 sites. As is expected by the electronegativity difference of lead and oxygen, electrons are transferred to oxygen atoms at all sites and coverages 0.06 ML to 1.00 ML. If the adsorbate layer is located above the surface, there is an excess of electrons outside the surface and an excess of positive charges inside the surface, leading to a negative dipole that reinforces the electron spill-out of the surface and increases the work function. However, when the adsorbate layer is close to the level of the top substrate layer, the sign of the work function change can be reversed, despite the transfer of electrons to the more electronegative atoms in the adsorbate layer.

To analyze the sign change of work function, the plane averaged electron difference $\Delta\rho(z)$ and the change in surface dipole moment density $\Delta p(z)$ are compared at the hollow and bridge sites at 1.00 ML coverage. From Fig. 3.9(b) it is known that the former system has lower work function than the clean Pb(100) surface, whereas the work function of the latter system is significantly higher. The change in surface dipole moment density $\Delta p(z)$ is defined as

$$\Delta p(z) = -\int_{z_0}^{z} z'\Delta\rho(z')\,\mathrm{d}z', \tag{3.4}$$

where $\Delta\rho(z') = \rho(z') - [\rho_s(z') + \rho_a(z')]$ is the charge density difference between the density of the whole system $\rho(z')$ and the densities of the substrate $\rho_s(z')$ and the adsorbates $\rho_a(z')$. The change in dipole density is linked to the change in work function ϕ via

$$\phi - \phi_0 = -\frac{e}{\epsilon_0}\left[\Delta p + (p_\mathrm{s} - p_0)\right], \tag{3.5}$$

where Δp is saturation value of the change in dipole density above the surface, and p_s and p_0 are the dipole densities of the relaxed substrate and the clean substrate, respectively [73].

The sign of $\Delta p(z)$ outside the surface is linked to the sign of work function change. Because $\Delta p(z)$ is essentially the sum of electron density difference weighted by z, even small changes in the electron density difference outside the surface can have a large effect on $\Delta p(z)$.

Figure 3.10(a) shows the electron density difference of oxygen on the hollow site at 1.00 ML coverage. The peak of electron accumulation is located

at the level of the top Pb layer, and an electron depletion peak (shown as a shaded area in Fig. 3.10(a)) is above the surface. When weighted by z and integrated, the depletion peak changes the sign of the dipole moment density (Fig. 3.10(b)) above the surface to a positive value. The work function of the structure is therefore lower than that of the clean surface.

On the bridge site (Fig. 3.10)(c) and (d)), the electron accumulation layer is at the level of the oxygen layer, more than 1 Å above the top Pb layer. This causes a decrease of Δp to a negative value, and since there is only a very small amount of electron depletion above the electron accumulation layer, the dipole moment density above the surface remains negative. The structure therefore has a higher work function than the clean surface.

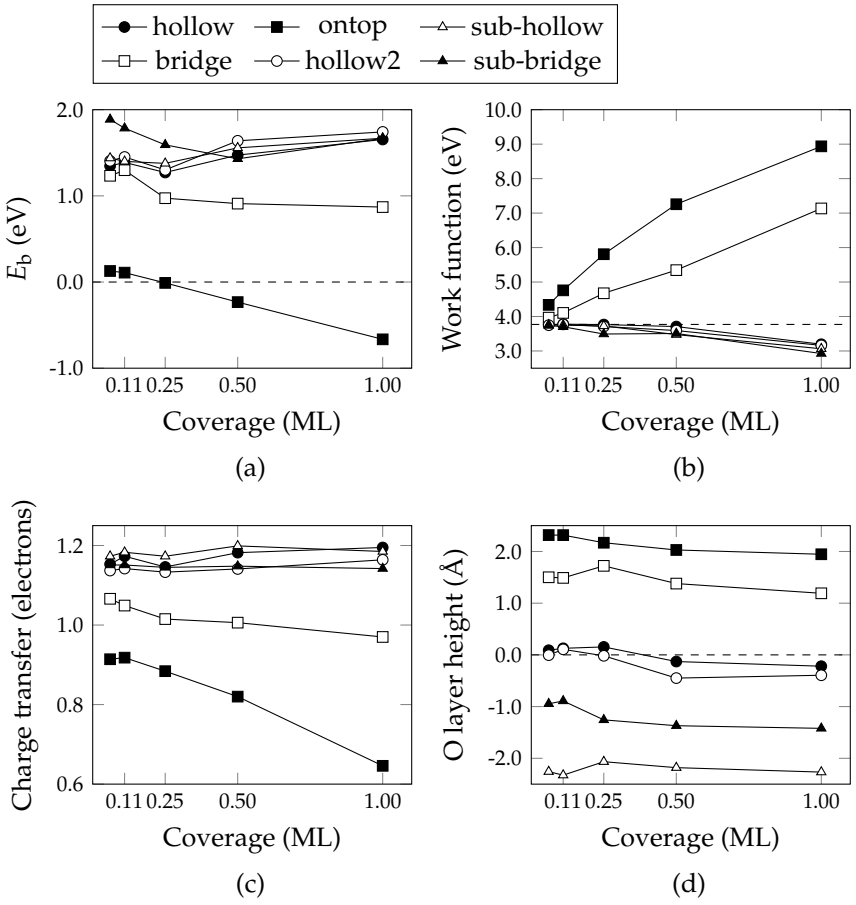

Figure 3.9: (a) Average oxygen binding energy (referenced to the O_2 molecule in the gas phase), (b) work function, (c) charge transfer and (d) average oxygen layer height of O adsorbed on Pb(100) at coverages 0.06 ML to 1.00 ML.

To elucidate the effect of oxygen adsorption on other oxygen atoms, the

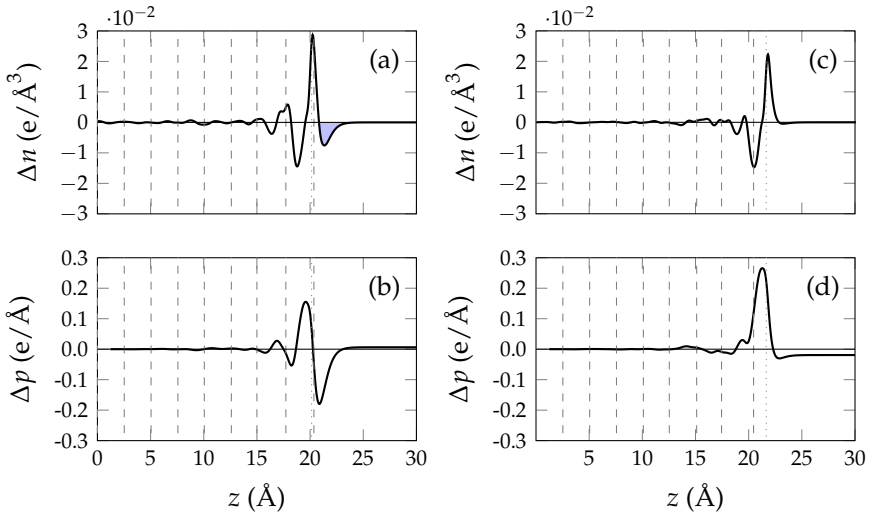

Figure 3.10: Valence electron density difference ((a) and (c)) and the corresponding change in dipole moment density (b) and (d) of oxygen adsorbed on Pb(100) at 1.00 ML coverage. (a) and (b): Oxygen on hollow site. (c) and (d): Oxygen on bridge site.

pairwise interactions of oxygen on adjacent hollow sites on the Pb(100) surfaces were studied. The initial configurations had oxygens on the hollow sites separated by an empty bridge site (Fig. 3.11(a)) and a Pb atom (Fig. 3.11(c)). Attractive interaction occurs for O separated by an empty bridge site with average oxygen binding energy 1.603 eV, approximately 0.15 eV higher than in the $p(3 \times 3)$ structure on the hollow2 site at a comparable coverage 0.11 ML. The oxygen atoms are pulled towards each other by 0.671 Å compared to the separation of the hollow sites.

The structure with oxygens separated by a Pb atom has repulsive interaction between the oxygen atoms. The binding energy is 1.382 eV, approximately 70 meV lower than for the hollow2 site in the $p(3 \times 3)$ structure. The O-O separation is 0.235 Å larger than the distance between the hollow sites. The valence electron density difference plots in Figs. 3.11(b) and 3.11(d) show that while electrons are accumulated near the O atoms in the axis connecting them when the O atoms are separated by an empty bridge site (Fig. 3.11(b)), electrons are depleted around the oxygen atoms in the direction connecting them to the Pb atom between the oxygens (Fig. 3.11(d)).

The attractive pairwise interaction and the binding energy increasing with coverage suggest that the oxide layer growth could proceed by e.g. island growth rather than through ordered overlayers. Such autocatalytic oxidation has been observed experimentally on Pb(111) [74]. To increase the number of nearest neighboring O atoms separated by a bridge site, a structure of parallel chains of O atoms was constructed, corresponding to cover-

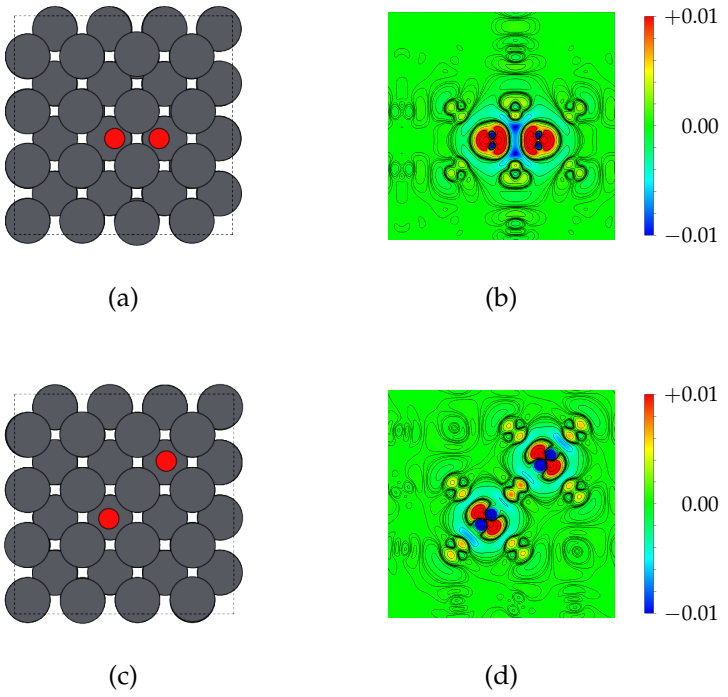

Figure 3.11: (a) Oxygen atoms separated by an empty bridge site and (b) the corresponding charge density difference. (c) Oxygen atoms separated by a Pb atom and (d) the corresponding charge density difference.

age 0.50 ML (Fig. 3.12). The average oxygen binding energy in this structure (1.809 eV) is 170 meV higher than the binding energy of the $c(2 \times 2)$ structure at coverage 0.50 ML.

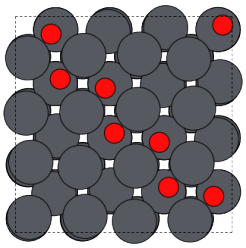

Figure 3.12: O/Pb(100) structure with parallel bands of oxygen at coverage 0.50 ML.

3.3.2 Surface oxide structure at two monolayers coverage

The formation of a multilayer oxide structure necessarily involves oxygen migration below the top substrate layer. In early experimental studies, the oxygen sticking probability was observed to decrease with increasing coverage, and the knee point of sticking has been estimated to occur at 1 ML coverage [75], 2 ML to 3 ML [76], and 2 ML or 6.3 Å oxide layer thickness [77]. This study was therefore limited to include no more than two layers of oxygen.

At low coverages, subsurface oxygen is thermodynamically more stable than on-surface oxygen. The energetically favoured site at coverages up to 0.25 ML is the subsurface bridge site, where the oxygen is located below the top Pb layer laterally in the same position as for on-surface adsorption on the bridge site. Another subsurface site considered here is the subsurface hollow site, where the oxygen is located directly below a top layer Pb atom. A NEB calculation (Fig. 3.13(a)) suggests that oxygen diffusion from an on-surface hollow site to a subsurface bridge site experiences no energy barrier at all, which indicates that oxygen diffuses readily below the top Pb layer. However, since the hollow site is stable and the oxygen does not spontaneously migrate to a subsurface bridge site during relaxation, a small energy barrier is likely located near the hollow site. The NEB calculations were unable to capture the barrier. Diffusion path from the subsurface bridge to the subsurface hollow site has an energy barrier of 0.56 eV at $\Theta = 0.11$ ML (Fig. 3.13(b)) .

Three candidates for the two monolayer surface oxide structure were constructed: a β-PbO structure, where the oxygen atoms occupy distorted hollow sites on and below the surface, an α-PbO structure, where the O atoms occupy bridge sites on and below the surface, and a hollow structure, where the O atoms are located on hollow sites both on and below the surface (see Fig. 3.14). The average oxygen binding energies are 2.184 eV for the β-PbO structure, 1.711 eV for the α-PbO structure, and 2.175 eV for the hollow structure. The β-PbO and hollow structures are very close in energy, and preferred to the α-PbO by a margin of ~ 460 meV per oxygen atom.

The stability of the structures was compared by vibrational frequency analysis, allowing only the oxygen atoms to vibrate, and keeping the substrate fixed. The α-PbO and β-PbO structures have real vibrational frequencies, while the hollow structure was found to have imaginary vibration modes, indicating that small displacements of the oxygen atoms from the hollow sites towards the β-PbO structure drives the structure to lower energy. The stable structure at two monolayers coverage is therefore the β-PbO structure, which is shown in Fig. 3.15. The calculated surface oxide layer thickness, $2.795\,\text{Å} + 3.519\,\text{Å} = 6.314\,\text{Å}$ compares well with the result obtained in experiments for oxidation of bulk lead ((6.3 ± 0.2) Å) [77].

The DOS projected on the surface oxide layer (Fig. 3.16(a)) shows Pb-O bonding resulting from the hybridization of Pb 6*s* and O 2*p* states around

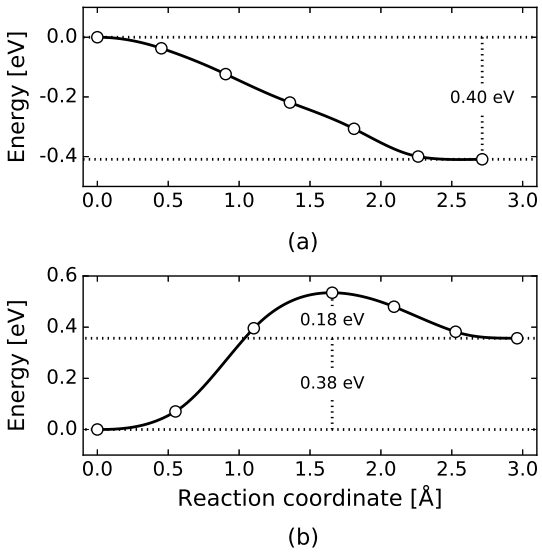

Figure 3.13: Oxygen diffusion pathways at coverage 0.11 ML. (a) From an on-surface hollow site to a subsurface bridge site. (b) From a subsurface bridge site to subsurface hollow site.

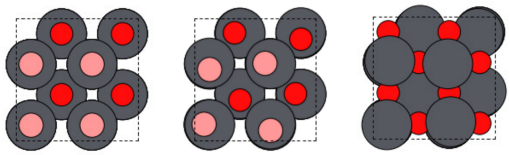

Figure 3.14: O/Pb(100) structures at 2.00 ML coverage. Oxygen atoms at (a) on-surface and subsurface hollow sites, (b) on-surface and subsurface hollow2 sites (β-PbO) and (c) on-surface and subsurface bridge sites (α-PbO). The light red circles mark the position of oxygen atoms below the top layer Pb atoms.

-8 eV. The origin of the distorted structure of bulk lead oxide has been discussed in an earlier study [78], and similar mechanism seems to be responsible for the distorted structure on the Pb(100) surface. The coupling of the $6s$ states of lead with the $2p$ states of oxygen mediates the hybridization of lead $6s$ and $6p$ states at the top of the valence band, which stabilizes the distorted structure. The distortion in the electron density around -2 eV is shown in Fig. 3.16(b).

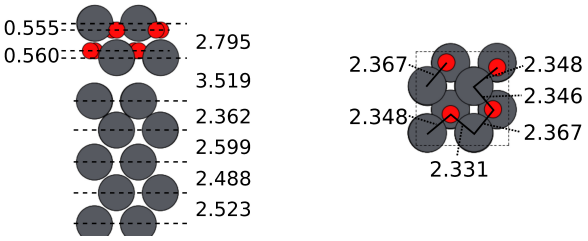

Figure 3.15: Interlayer spacings and Pb-O bond lengths of the stable oxide structure at two monolayers coverage.

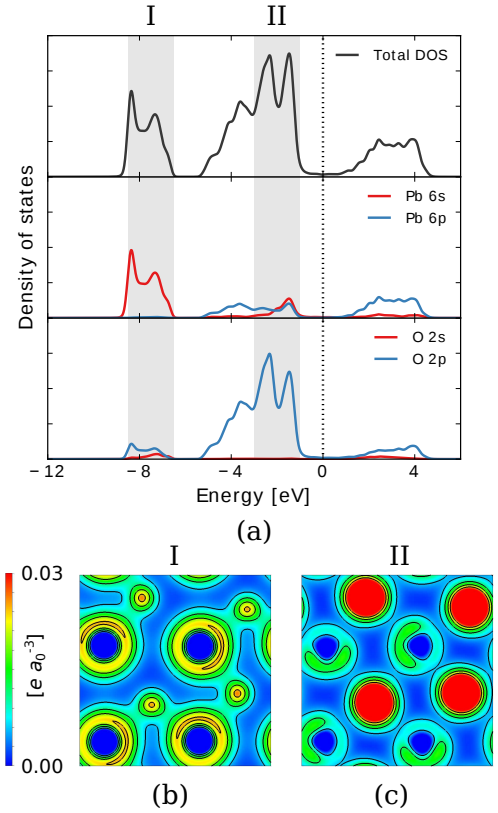

Figure 3.16: (a) Density of states projected on the Pb and O layers of the β-PbO overlayer on Pb(100). Top: Total DOS of the PbO layer. Middle: The $6s$ (red) and $6p$ states (blue) of the Pb atoms. Bottom: The $2s$ (red) and $2p$ states (blue) of the O atoms. The dotted vertical line marks the Fermi level. (b) Partial charge density at the bottom of the valence band ($-8.5\,$eV to $-6.5\,$eV). (c) Partial charge density at the top of the valence band ($-3.0\,$eV to $-1.0\,$eV).

CHAPTER 4

Concluding remarks

This thesis consists of three publications, where elementary surface-adsorbate interactions such as adsorption, dissociation, diffusion, and vibration are discussed.

Firstly, ambiguities considering the adsorption of molecular and atomic oxygen on Ag(110) are clarified. We have shown that the preferred orientation of the molecule is along the rows of the Ag(110) surface, and the dissociation of the molecule is facilitated by coupling to a surface phonon mode. Atomic oxygen then preferably occupies fourfold hollow or threefold hollow sites, contrary to previous view of occupying short bridge sites. Oxygen adsorption on the Ag(110) surface induces a small peak below the Fermi level in the Ag *d*-projected DOS, which generally enhances the reactivity of the surface.

Secondly, complementary DFT calculations to LEED experiments are presented. The results together confirm that potassium forms a $c(2 \times 2)$ structure on lead (100) surface, with the potassium atoms occupying substitutional sites. Potassium adsorption is shown to lead to a decrease of work function, which is expected to result in increased binding energy of electron-acceptor adsorbates, such as oxygen.

Thirdly, oxygen adsorption on lead (100) surface is shown to result in a surface oxide layer with the oxygen atoms occupying distorted hollow sites, where the distortion arises from electronic effects mediated by oxygen. The adsorption site dependent trends in work function and binding energy are related to electron distribution at the surface layer and the resulting surface dipole. Oxygen adsorption is shown to have directional preference at low coverages, which indicates that also the oxide layer formation can have strong directional dependence. Although the clean and defect-free lead surfaces are resistant to oxidation, adsorbed oxygen can facilitate O_2 dissociation on the surface, as discussed by Thürmer et al. [74].

Some aspects that remain open for further study are the possible increase of catalytic activity of the Ag(110) surface due to the oxygen-induced peak in the density of states near the Fermi level, and how it evolves with oxygen coverage. The effect of imperfections, such as vacancies or adatoms, on the oxidation of the Pb(100) surface warrants further investigation, as

they are potential nucleation sites for surface oxide growth. However, the whole surface oxide layer growth process, from the dissociation of the O_2 molecule to the presumably simultaneous on-surface and subsurface adsorption, is very demanding to simulate computationally. Also, the effect of alkali impurities on Pb(100) oxidation could be significant, since potassium adsorption lowers the work function of the Pb(100) surface, and is therefore expected to facilitate oxygen adsorption.

References

[1] A. Groß. *Theoretical surface science: a microscopic perspective*. Springer-Verlag, Berlin Heidelberg, 2009. ISBN 978-3-540-68966-9.

[2] O. Deutschmann, H. Knözinger, K. Kochloefl, & T. Turek. *Heterogeneous Catalysis and Solid Catalysts*. Wiley-VCH Verlag, 2000. ISBN 978-3-527-30673-2.

[3] S. Royer & D. Duprez. Catalytic oxidation of carbon monoxide over transition metal oxides. *ChemCatChem*, **3**(1):24, 2011.

[4] C. G. Vayenas, S. Bebelis, & S. Ladas. Dependence of catalytic rates on catalyst work function. *Nature*, **343**:625, 1990.

[5] P. Hohenberg & W. Kohn. Inhomogeneous electron gas. *Physical Review*, **136**:864, 1964.

[6] W. Kohn & L. J. Sham. Self-consistent equations including exchange and correlation effects. *Physical Review*, **140**:1133, 1965.

[7] M. E. Ali, M. M. Rahman, S. M. Sarkar, & S. B. Abd Hamid. Heterogeneous metal catalysts for oxidation reactions. *Journal of Nanomaterials*, **2014**:192038, 2014.

[8] K. C. Salooja. Decomposition of peroxides by lead oxides: Accompanying changes in the nature of lead oxides. *Combustion and Flame*, **12**(4):302, 1968.

[9] K. Asami, T. Shikada, K. Fujimoto, & H. Tominaga. Oxidative coupling of methane over lead oxide catalyst: kinetic study and reaction mechanism. *Industrial & Engineering Chemistry Research*, **26**(11):2348, 1987.

[10] G. Wendt, C.-D. Meinecke, & W. Schmitz. Oxidative dimerization of methane on lead oxide–alumina catalysts. *Applied Catalysis*, **45**(2):209, 1988.

[11] S. Kurth, J. P. Perdew, & P. Blaha. Molecular and solid-state tests of density functional approximations: LSD, GGAs, and meta-GGAs. *International Journal of Quantum Chemistry*, **75**:889, 1999.

[12] R. M. Martin. *Electronic structure: basic theory and practical methods*. Cambridge University Press, Cambridge, UK, 2004. ISBN 978-0-521-78285-2.

[13] P. E. Blöchl. Projector augmented-wave method. *Physical Review B*, **50**:17953, 1994.

[14] G. Kresse & J. Hafner. Ab initio molecular dynamics for liquid metals. *Physical Review B*, **47**:558, 1993.

[15] G. Kresse & J. Hafner. Ab initio molecular-dynamics simulation of the liquid-metal–amorphous-semiconductor transition in germanium. *Physical Review B*, **49**:14251, 1994.

[16] G. Kresse & J. Furthmüller. Efficiency of ab-initio total energy calculations for metals and semiconductors using a plane-wave basis set. *Computational Materials Science*, **6**:15, 1996.

[17] G. Kresse & J. Furthmüller. Efficient iterative schemes for ab initio total-energy calculations using a plane-wave basis set. *Physical Review B*, **54**:11169, 1996.

[18] G. Kresse & D. Joubert. From ultrasoft pseudopotentials to the projector augmented-wave method. *Physical Review B*, **59**:1758, 1999.

[19] R. F. W. Bader. *Atoms in molecules: a quantum theory*. Clarendon Press, 1994. ISBN 9780198558651.

[20] G. Mills & H. Jónsson. Quantum and thermal effects in H_2 dissociative adsorption: Evaluation of free energy barriers in multidimensional quantum systems. *Physical Review Letters*, **72**:1124, 1994.

[21] G. Mills, H. Jónsson, & G. K. Schenter. Reversible work transition state theory: Application to dissociative adsorption of hydrogen. *Surface Science*, **324**:305, 1995.

[22] G. Henkelman, B. P. Uberuaga, & H. Jónsson. A climbing image nudged elastic band method for finding saddle points and minimum energy paths. *Journal of Chemical Physics*, **113**:9901, 2000.

[23] D. Sholl & J. A. Steckel. *Density functional theory: a practical introduction*. John Wiley & Sons, Inc., Hoboken, New Jersey, 2009. ISBN 978-0-470-37317-0.

[24] N. W. Ashcroft & N. D. Mermin. *Solid state physics*. Saunders College Publishing, Fort Worth, 1976. ISBN 0-03-083993-9.

[25] P. Haas, F. Tran, & P. Blaha. Calculation of the lattice constant of solids with semilocal functionals. *Physical Review B*, **79**:085104, 2009.

[26] F. D. Murnaghan. The compressibility of media under extreme pressures. *Proceedings of the National Academy of Sciences of the United States of America*, **30**:244, 1944.

[27] F. Birch. Finite elastic strain of cubic crystals. *Physical Review*, **71**:809, 1947.

[28] R. Gaudoin & W. M. C. Foulkes. Ab initio calculations of bulk moduli and comparison with experiment. *Physical Review B*, **66**:052104, 2002.

[29] L. Lefferts, J. G. van Ommen, & J. R. H. Ross. The oxidative dehydrogenation of methanol to formaldehyde over silver catalysts in relation to the oxygen-silver interaction. *Applied Catalysis*, **23**:385, 1986.

[30] L. Savio, A. Gerbi, L. Vattuone, M. Rocca, F. Vecchiocattivi, D. Cappelletti, & F. Pirani. Heterolitic photolysis of O_2 on Ag(100). *Chemical Physics Letters*, **404**:336, 2005.

[31] J. G. Serafin, A. C. Liu, & S. R. Seyedmonir. Surface science and the silver-catalyzed epoxidation of ethylene: an industrial perspective. *Journal of Molecular Catalysis A: Chemical*, **131**(1-3):157, 1998.

[32] C. T. Campbell & M. T. Paffett. Model studies of ethylene epoxidation catalyzed by the Ag(110) surface. *Surface Science*, **139**(2-3):396, 1984.

[33] C. Wen, A. Yin, & W.-L. Dai. Recent advances in silver-based heterogeneous catalysts for green chemistry processes. *Applied Catalysis B: Environmental*, **160-161**:730, 2014.

[34] P. A. Gravil & D. M. Bird. Adsorption and dissociation of O_2 on Ag(110). *Physical Review Letters*, **77**(18):3933, 1996.

[35] F. E. Olsson, N. Lorente, & M. Persson. STM images of molecularly and atomically chemisorbed oxygen on silver. *Surface Science*, **522**(1-3):L27, 2003.

[36] P. J. van den Hoek & E. J. Baerends. Chemisorption and dissociation of O_2 on Ag(110). *Surface Science*, **221**(3):L791, 1989.

[37] S. Monturet, M. Alducin, & N. Lorente. Role of molecular electronic structure in inelastic electron tunneling spectroscopy: O_2 on Ag(110). *Physical Review B*, **82**(8):085447, 2010.

[38] J. R. Hahn & W. Ho. Chemisorption and dissociation of single oxygen molecules on Ag(110). *The Journal of Chemical Physics*, **123**(21):214702, 2005.

[39] J. Pal, T. B. Rawal, M. Smerieri, S. Hong, M. Alatalo, L. Savio, L. Vattuone, T. S. Rahman, & M. Rocca. Adatom extraction from pristine metal terraces by dissociative oxygen adsorption: combined STM and density functional theory investigation of O/Ag(110). *Physical Review Letters*, **118**(22):226101, 2017.

[40] K. C. Prince, G. Paolucci, & A. M. Bradshaw. Oxygen adsorption on silver (110): Dispersion, bonding and precursor state. *Surface Science*, **175**(1):101, 1986.

[41] S. W. Hla, P. Lacovig, G. Comelli, A. Baraldi, M. Kiskinova, & R. Rosei. Orientational anisotropy in oxygen dissociation on Rh(110). *Physical Review B*, **60**(11):7800, 1999.

[42] S. Y. Liem, J. H. R. Clarke, & G. Kresse. Pathways to dissociation of O_2 on Cu(110) surface: first principles simulations. *Surface Science*, **459**(1-2):104, 2000.

[43] R. Tatarek, G. Bracco, F. Tommasini, A. Franchini, V. Bortolani, G. Santoro, & R. F. Wallis. Surface resonant phonons of Ag(110). *Surface Science*, **211-212**:314, 1989.

[44] G. Bracco, L. Bruschi, L. Pedemonte, & R. Tatarek. Temperature dependence of the Ag(110) surface phonons. *Surface Science*, **377-379**:325, 1997.

[45] L. Yang, T. S. Rahman, G. Bracco, & R. Tatarek. Missing-row reconstruction of Ag(110) induced by a $p(2 \times 1)$ oxygen overlayer. *Physical Review B*, **40**:12271, 1989.

[46] L. Yang & T. S. Rahman. Surface phonon dispersion of Ag(110). *Surface Science*, **215**:147, 1989.

[47] S. Narasimhan. Ab initio lattice dynamics of Ag(1 1 0). *Surface Science*, **496**:331, 2002.

[48] F. Bartolucci, R. Franchy, J. C. Barnard, & R. E. Palmer. Two chemisorbed species of O_2 on Ag(110). *Physical Review Letters*, **80**:5224, 1998.

[49] L. Vattuone, U. Valbusa, & M. Rocca. Coverage dependence of the O-Ag(110) vibration. *Surface Science*, **317**:L1120, 1994.

[50] C.Åkerlund, I. Zorić, B. Kasemo, A. Cupolillo, F. B. de Mongeot, & M. Rocca. Dissociation of O_2 chemisorbed on Ag(110) and Pt(111) induced by energetic Xe atoms. *Chemical Physics Letters*, **270**:157, 1997.

[51] R. W. Gurney. Theory of electrical double layers in adsorbed films. *Physical Review*, **47**:479, 1935.

[52] N. D. Lang. Theory of work-function changes induced by alkali adsorption. *Physical Review B*, **4**:4234, 1971.

[53] N. D. Lang. The density-functional formalism and the electronic structure of metal surfaces. *Solid State Physics*, **28**:225, 1973.

[54] N. D. Lang & A. R. Williams. Self-consistent theory of the chemisorption of H, Li, and O on a metal surface. *Physical Review Letters*, **34**:531, 1975.

[55] N. D. Lang & A. R. Williams. Theory of atomic chemisorption on simple metals. *Physical Review B*, **18**:616, 1978.

[56] J. P. Muscat & D. M. Newns. Chemisorption on metals. *Progress in Surface Science*, **9**:1, 1978.

[57] J. P. Muscat & D. M. Newns. The interpretation of work-function variation in alkali chemisorption from the atomic viewpoint. *Journal of Physics C: Solid State Physics*, **7**:2630, 1974.

[58] A. Schmalz, S. Aminpirooz, L. Becker, J. Haase, J. Neugebauer, M. Scheffler, D. R. Batchelor, D. L. Adams, & E. Bøgh. Unusual

chemisorption geometry of Na on Al(111). *Physical Review Letters*, **67**:2163, 1991.

[59] J. Neugebauer & M. Scheffler. Adsorbate-substrate and adsorbate-adsorbate interactions of Na and K adlayers on Al(111). *Physical Review B*, **46**:16067, 1992.

[60] M. Kerkar, D. Fisher, D. P. Woodruff, R. G. Jones, R. D. Diehl, & B. Cowie. Structural study of alkali/simple metal adsorption: Rb and Na on Al(111). *Physical Review Letters*, **68**:3204, 1992.

[61] H. Over, H. Bludau, M. Skottke-Klein, G. Ertl, W. Moritz, & C. T. Campbell. Coverage dependence of adsorption-site geometry in the Cs/Ru(0001) system: A low-energy electron-diffraction analysis. *Physical Review B*, **45**:8638, 1992.

[62] J. Neugebauer & M. Scheffler. Mechanisms of island formation of alkali-metal adsorbates on Al(111). *Physical Review Letters*, **71**:577, 1993.

[63] C. Stampfl & M. Scheffler. Theoretical identification of a (2×2) composite double layer ordered surface alloy of Na on Al(111). *Surface Science*, **319**:L23, 1994.

[64] A. Politano, G. Chiarello, G. Benedek, E. V. Chulkov, & P. M. Echenique. Vibrational spectroscopy and theory of alkali metal adsorption and co-adsorption on single-crystal surfaces. *Surface Science Reports*, **68**:305, 2013.

[65] M. S. Altman & E. Bauer. The reconstructions of the Pb(110) surface studied by low energy electron microscopy. *Surface Science*, **344**:51, 1995.

[66] F. M. Pan, M. Caragiu, N. Ferralis, & R. D. Diehl. Substitutional adsorption geometry for Pb(111)–$(\sqrt{3} \times \sqrt{3})$R30°–K. *Surface Science*, **600**:537, 2006.

[67] K. C. Prince. Adsorption of potassium on Pb(110). *Surface Science*, **193**:L24, 1988.

[68] V. Fiorentini & M. Methfessel. Extracting convergent surface energies from slab calculations. *Journal of Physics: Condensed Matter*, **8**:6525, 1996.

[69] J. S. Casas & J. Sordo, editors. *Lead: chemistry, analytical aspects, environmental impact and health effects*. Elsevier, Amsterdam, 2006. ISBN 978-0-444-52945-9.

[70] L. M. Droessler, H. E. Assender, & A. A. R. Watt. Thermally deposited lead oxides for thin film photovoltaics. *Materials Letters*, **71**:51, 2012.

[71] A. F. Wells. *Structural Inorganic Chemistry*. Oxford University Press, Oxford, 5th edition, 2012. ISBN 978-0-19-965763-6.

[72] B. Predel. O-Pb (oxygen-lead): Datasheet from Landolt-Börnstein - group IV physical chemistry · volume 5I: "Ni-Np – Pt-Zr" in SpringerMaterials. Copyright 1998 Springer-Verlag Berlin Heidelberg.

[73] T. C. Leung, C. L. Kao, W. S. Su, Y. J. Feng, & C. T. Chan. Relationship between surface dipole, work function and charge transfer: Some exceptions to an established rule. *Physical Review B*, **68**:195408, 2003.

[74] K. Thürmer, E. Williams, & J. Reutt-Robey. Autocatalytic oxidation of lead crystallite surfaces. *Science*, **297**:2033, 2002.

[75] S. Evans & J. M. Thomas. Electronic structure of the oxides of lead. Part 1.—A study using X-ray and ultraviolet photoelectron spectroscopy of polycrystalline lead. *Journal of the Chemical Society, Faraday Transactions II*, **71**:313, 1975.

[76] D. Chadwick & A. B. Christie. Oxidation of polycrystalline and (111) lead surfaces studied by electron spectroscopy. *Journal of the Chemical Society, Faraday Transactions II*, **76**:267, 1980.

[77] N. J. Chou, J. M. Eldridge, R. Hammer, & D. Dong. Auger and ellipsometric studies of ultra-thin PbO growth on lead. *Journal of Electronic Materials*, **2**:115, 1973.

[78] D. J. Payne, R. G. Egdell, A. Walsh, G. W. Watson, J. Guo, P.-A. Glans, T. Learmonth, & K. E. Smith. Electronic origins of structural distortions in post-transition metal oxides: Experimental and theoretical evidence for a revision of the lone pair model. *Physical Review Letters*, **96**:157403, 2006.

Publication I

T. B. Rawal, S. Hong, A. Pulkkinen, M. Alatalo and T. S. Rahman
Adsorption, diffusion and vibration of oxygen on Ag(110)

Reprinted from *Physical Review B*, 92(3), pp. 035444,

Publication II

Y.-T. Huang, R. D. Diehl, A. Pulkkinen and K. Pussi
Low-energy electron diffraction and density functional theory study of potassium adsorbed on Pb(100)

Reprinted from *Journal of Physics: Condensed Matter*, 27(34), pp. 345001,

Publication III

A. Pulkkinen and K. Pussi
Atomic oxygen adsorption on Pb(100)

Reprinted from *The European Physical Journal B*, 90(10), pp. 184, © 2017, with permission of Springer.

ACTA UNIVERSITATIS LAPPEENRANTAENSIS

748. ALI-MARTTILA, MAAREN. Towards successful maintenance service networks – capturing different value creation strategies. 2017. Diss.

749. KASHANI, HAMED TASALLOTI. On dissimilar welding: a new approach for enhanced decision-making. 2017. Diss.

750. MVOLA BELINGA, ERIC MARTIAL. Effects of adaptive GMAW processes: performance and dissimilar weld quality. 2017. Diss.

751. KARTTUNEN, JUSSI. Current harmonic compensation in dual three-phase permanent magnet synchronous machines. 2017. Diss.

752. SHI, SHANSHUANG. Development of the EAST articulated maintenance arm and an algorithm study of deflection prediction and error compensation. 2017. Diss.

753. CHEN, JIE. Institutions, social entrepreneurship, and internationalization. 2017. Diss.

754. HUOTARI, PONTUS. Strategic interaction in platform-based markets: An agent-based simulation approach. 2017. Diss.

755. QU, BIN. Water chemistry and greenhouse gases emissions in the rivers of the "Third Pole" / Water Tower of Asia". 2017. Diss.

756. KARHU, PÄIVI. Cognitive ambidexterity: Examination of the cognitive dimension in decision-making dualities. 2017. Diss.

757. AGAFONOVA, OXANA. A numerical study of forest influences on the atmospheric boundary layer and wind turbines. 2017. Diss.

758. AZAM, RAHAMATHUNNISA MUHAMMAD. The study of chromium nitride coating by asymmetric bipolar pulsed DC reactive magnetron sputtering. 2017. Diss.

759. AHI, MOHAMADALI. Foreign market entry mode decision-making: Insights from real options reasoning. 2017. Diss.

760. AL HAMDI, ABDULLAH. Synthesis and comparison of the photocatalytic activities of antimony, iodide and rare earth metals on SnO2 for the photodegradation of phenol and its intermediates under UV, solar and visible light irradiations. 2017. Diss.

761. KAUTTO, JESSE. Evaluation of two pulping-based biorefinery concepts. 2017. Diss.

762. AFZALIFAR, ALI. Modelling nucleating flows of steam. 2017. Diss.

763. VANNINEN, HEINI. Micromultinationals - antecedents, processes and outcomes of the multinationalization of small- and medium-sized firms. 2017. Diss.

764. DEVIATKIN, IVAN. The role of waste pretreatment on the environmental sustainability of waste management. 2017. Diss.

765. TOGHYANI, AMIR. Effect of temperature on the shaping process of an extruded wood-plastic composite (WPC) profile in a novel post-production process. 2017. Diss.

766. LAAKKONEN, JUSSI. An approach for distinct information privacy risk assessment. 2017. Diss.

767. KASURINEN, HELI. Identifying the opportunities to develop holistically sustainable bioenergy business. 2017. Diss.

768. KESKISAARI, ANNA. The impact of recycled raw materials on the properties of wood-plastic composites. 2017. Diss.

769. JUKKA, MINNA. Perceptions of international buyer-supplier relational exchange. 2017. Diss.

770. BAYGILDINA, ELVIRA. Thermal load analysis and monitoring of doubly-fed wind power converters in low wind speed conditions. 2017. Diss.

771. STADE, SAM. Examination of the compaction of ultrafiltration membranes with ultrasonic time-domain reflectometry. 2017. Diss.

772. KOZLOVA, MARIIA. Analyzing the effects of a renewable energy support mechanism on investments under uncertainty: case of Russia. 2017. Diss.

773. KURAMA, ONESFOLE. Similarity based classification methods with different aggregation operators. 2017. Diss.

774. LYYTIKÄINEN, KATJA. Removal of xylan from birch kraft pulps and the effect of its removal on fiber properties, colloidal interactions and retention in papermaking. 2017. Diss.

775. GAFUROV, SALIMZHAN. Theoretical and experimental analysis of dynamic loading of a two-stage aircraft engine fuel pump and methods for its decreasing. 2017. Diss.

776. KULESHOV, DMITRII. Modelling the operation of short-term electricity market in Russia. 2017. Diss.

777. SAARI, JUSSI. Improving the effectiveness and profitability of thermal conversion of biomass. 2017. Diss.

778. ZHAO, FEIPING. Cross-linked chitosan and β-cyclodextrin as functional adsorbents in water treatment. 2017. Diss.

779. KORHONEN, ILKKA. Mobile sensor for measurements inside combustion chamber – preliminary study. 2017. Diss.

780. SIKIÖ, PÄIVI. Dynamical tree models for high Reynolds number turbulence applied in fluid-solid systems of 1D-space and time. 2017. Diss.

781. ROMANENKO, ALEKSEI. Study of inverter-induced bearing damage monitoring in variable-speed-driven motor systems. 2017. Diss.

782. SIPILÄ, JENNI. The many faces of ambivalence in the decision-making process. 2017. Diss.

783. HAN, MEI. Hydrodynamics and mass transfer in airlift bioreactors; experimental and numerical simulation analysis. 2017. Diss.

784. ESCALANTE, JOHN BRUZZO. Dynamic simulation of cross-country skiing. 2017. Diss.

785. NOKKA, JARKKO. Energy efficiency analyses of hybrid non-road mobile machinery by real-time virtual prototyping. 2017. Diss.

786. VUORIO, ANNA. Opportunity-specific entrepreneurial intentions in sustainable entrepreneurship. 2017. Diss.